Science of Remote Sensing 12 (2025) 100248

Contents lists available at ScienceDirect

Science of Remote Sensing

journal homepage: www.sciencedirect.com/journal/science-of-remote-sensing

Full length article

Refining satellite laser altimetry geolocation through full-waveform radiative transfer modeling and matching

Ameni Mkaouar [a,d,*], David Shean [b], Tiangyang Yin [c,**], Christopher S.R. Neigh [d], Rodrigo Vieira Leite [d], Paul M. Montesano [e,f], Abdelaziz Kallel [g], Jean-Phillipe Gastellu-Etchegorry [h]

[a] Goddard Earth Sciences Technology and Research II, University of Maryland Baltimore County, Baltimore, 21228, MD, USA
[b] Department of Civil and Environmental Engineering, University of Washington, Seattle, 98195, WA, USA
[c] Department of Land Surveying and Geo-Informatics, The Hong Kong Polytechnic University, Hung Hom, Hong Kong
[d] Biospheric Sciences Laboratory, NASA Goddard Space Flight Center, Greenbelt, 20771, MD, USA
[e] ADNET Systems, Inc., Bethesda, 20817, MD, USA
[f] Office of Computational and Information Sciences and Technology, NASA Goddard Space Flight Center, Greenbelt, 20771, MD, USA
[g] Signals, Systems Artificial Intelligence and Networks (SM@RTS) laboratory, Digital Research Center of Sfax, 3021, Sfax, Tunisia
[h] Centre d'Etudes Spatiales de la Biosphere– UT3, CNES, CNRS, IRD, Universite de Toulouse, 31401, Toulouse, France

ARTICLE INFO

Dataset link: https://gliht.gsfc.nasa.gov/, www.cesbio.ups-tlse.fr/dart

Keywords:
GEDI
Geolocation
Waveform-matching
Simulation
LiDAR
Surface topography
Vegetation
Radiative transfer
3D modeling
DART
Ray tracing

ABSTRACT

Advances in geolocation accuracy for spaceborne laser altimetry data are critical for numerous applications. Existing methods often address the problem on a global scale, primarily relying on ground returns and overlooking the effects of vegetation canopy, which can lead to inaccuracies, especially when integrating these data with other georeferenced datasets. We developed a novel, site-focused approach to evaluate and correct geolocation errors in full-waveform spaceborne laser altimeter data using simulated data from the 3D discrete anisotropic radiative transfer (DART) model. Our analysis operates at the scale of a LiDAR footprint, employing waveform matching that effectively accounts for both vegetation and ground returns across various forest types. We used DART to (i) prepare realistic 3D vegetation scenes reconstructed from dense ($> 20\,pt/m^2$), small footprint airborne LiDAR data, and (ii) simulate Global Ecosystem Dynamics Investigation (GEDI) waveforms within these scenes. Our approach determines the "true" GEDI footprint positions by maximizing the similarity between simulated and observed GEDI full-waveforms within a local search area. We evaluated this method across various sites with different forest canopy types, finding strong correlations between simulated and observed GEDI waveforms ($r^2 \in [0.94, 0.99]$) and root mean square errors (RMSE) $\in [0.14, 0.63]$. Random GEDI geolocation errors ranged from 5-10 m, and systematic errors were less than 8 m, within the GEDI product specification. Waveform matching was most successful for complex waveforms over heterogeneous, open canopies, and less effective for homogeneous, closed canopies over flat terrain. Our approach offers improved performance, with lower RMSE and higher correlation, over existing ALS-basedmethods. These advances support spaceborne data fusion through precise integration of vertical vegetation structure profiles from laser altimetry with horizontal vegetation structure of canopy and ground surface topography.

1. Introduction

Spaceborne laser altimetry or Light Detection and Ranging (LiDAR) instruments have set a new standard for precise Earth surface elevation measurements in recent decades. From monitoring climate variables (Magruder et al., 2024), to tracking dynamics of glaciers and ice sheets (Zhang et al., 2023; Chartrand and Howat, 2023), to assessing water levels (Fayad et al., 2020; Menounos et al., 2023), and even mapping the vast complexity of forest ecosystems (Musthafa et al., 2023), LiDAR has become an indispensable tool. Its precise elevation measurements not only enhance our understanding of natural processes but also provide critical insights into ecosystems, biodiversity, and climate change.

* Corresponding author at: Biospheric Sciences Laboratory, NASA Goddard Space Flight Center, Greenbelt, 20771, MD, USA.
** Corresponding author.
E-mail addresses: ameni.mkaouar@nasa.gov (A. Mkaouar), tiangang.yin@polyu.edu.hk (T. Yin).

https://doi.org/10.1016/j.srs.2025.100248
Received 23 October 2024; Received in revised form 30 April 2025; Accepted 12 June 2025
Available online 24 June 2025

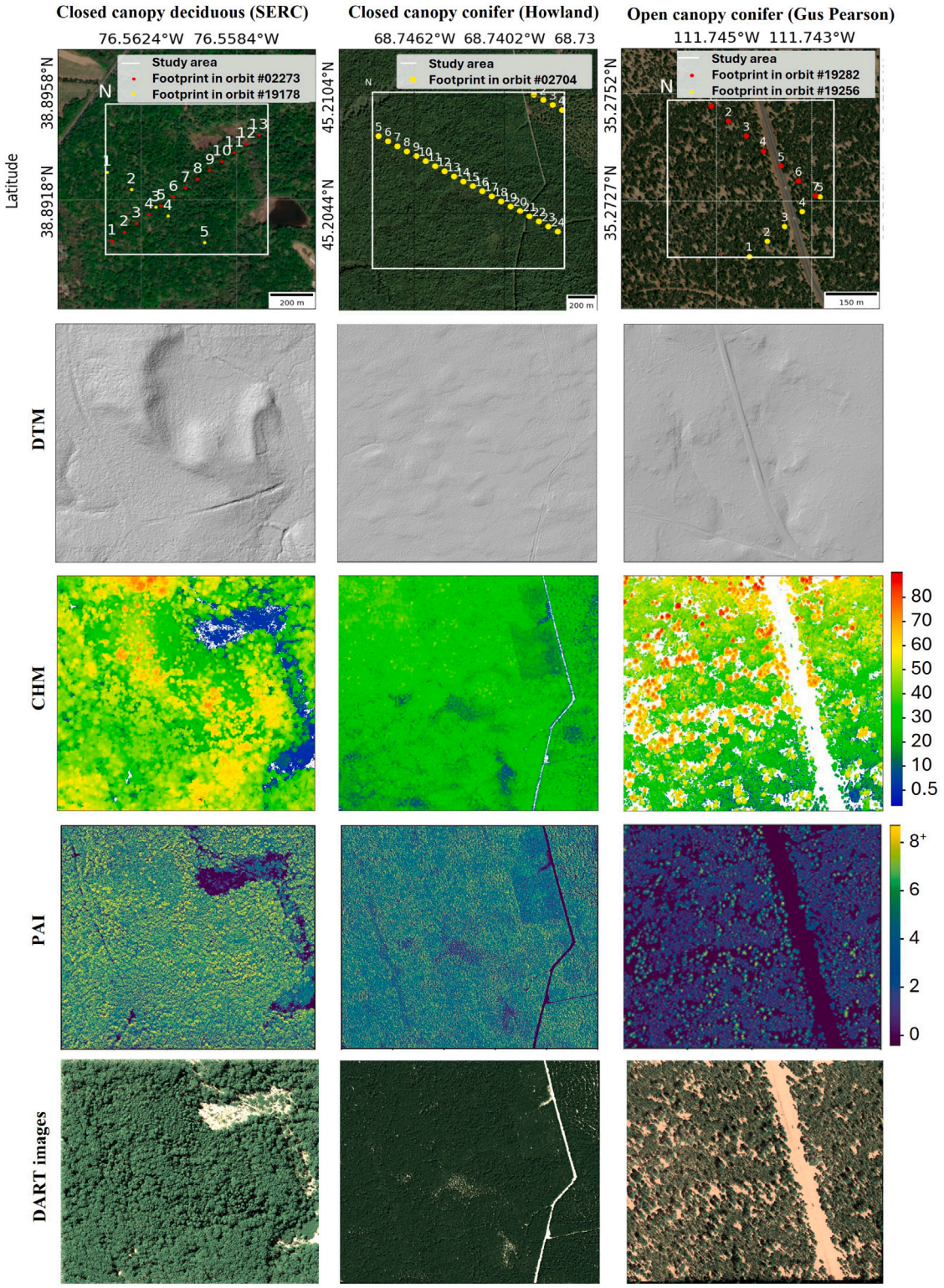

Fig. 1. The three study areas with GEDI Footprint locations plotted on ESRI World Imagery basemaps[1] (top row), metrics derived from airborne LiDAR data (middle rows), and simulated RGB satellite images (bottom row). White squares indicate the extent of each simulated forest scene: (closed canopy deciduous (SERC), 600 × 600 m), (closed canopy coniferous (Howland), 1000 × 1000 m), and (open canopy coniferous (Gus Pearson), 400 × 400 m). Yellow and red dots mark available ground tracks for GEDI Level-1B footprints with longitude/latitude coordinates of the "last-bin" returns. The 1 m Digital Terrain Model (DTM) and Canopy Height Model (CHM) products were prepared from NASA G-LiHT airborne LiDAR data and the Plant Area Index (PAI) maps were estimated using the PVlad model. The RGB satellite images were simulated with nadir view using DART for each reconstructed scene.

The geolocation accuracy of laser altimetry data is a crucial metric for instrument performance, with implications for meeting primary mission science objectives and instilling confidence within the research community. Precise footprint geolocation enables reliable estimates of

[1] ESRI. "World Imagery". https://www.arcgis.com/home/item.html?id=10df2279f9684e4a9f6a7f08febac2a9.

forest structure (Roy et al., 2021; Sun et al., 2022) and facilitates integration with other georeferenced datasets, thus supporting diverse applications such as snow depth assessments (Shean et al., 2021) and the generation of global digital terrain models (DTMs) (Magruder et al., 2021). However, various factors, such as platform vibrations, orbit adjustment maneuvers, and dynamic environmental elements, can introduce errors in instrument position and pointing, leading to both systematic and random footprint geolocation inaccuracies on the ground (Dennehy and Alvarez-Salazar, 2019). To mitigate these challenges, iterative instrument calibration and independent evaluations of geolocation accuracy are paramount for ensuring the reliability and accuracy of laser altimetry measurements, and enhancing their contribution to fusion activities with other spaceborne data

1.1. GEDI satellite laser altimetry

The NASA Global Ecosystem Dynamics Investigation (GEDI) mission enhances our understanding of Earth's ecosystems by collecting systematic measurements of the Earth's surface and vegetation structure. It launched in 2018 and began operations aboard the International Space Station (ISS) in April 2019, with near-global coverage from 51.6° south to 51.6° north. The primary GEDI science objectives involve forest above-ground biomass (AGB) quantification, land surface carbon budget modeling, and vegetation structure estimation (Hancock et al., 2019; Schneider et al., 2020; Dubayah et al., 2022; Crockett et al., 2023).

The GEDI instrument includes three 1064 nm (near-infrared) lasers that emit 14 ns laser pulses with a power of 10 mJ and a pulse repetition rate of 242 Hz. Two lasers operate at full power, while the third is split into two "coverage" beams, each operating at half power. These four beams are further split by beam dithering units, producing eight ground tracks with cross-track spacing of 600 m. Each individual footprint is circular and 25 m in diameter, with along-track spacing of 60 m. The LiDAR return waveforms are recorded for each footprint and subsequently processed to generate GEDI data products at the footprint level (Dubayah et al., 2020b).

GEDI footprint geolocation relies on a combination of onboard sensors, including its inertial measurement unit (IMU), global navigation satellite system (GNSS) receiver, and three star trackers (Dubayah et al., 2020a). Nevertheless, the ISS has many distinctive characteristics, including a relatively low orbit (i.e., average altitude of 400 km), complex platform configuration, and many dynamic systems. The latter can introduce mechanical vibrations in the GEDI instrument, often referred to as "jitter", which introduce fluctuations in orientation. Consequently, these variations can impact the accuracy and precision of horizontal position measurements (Schneider et al., 2020; Xu et al., 2023a).

1.2. Assessing and correcting geolocation accuracy in spaceborne LiDAR full waveform data

Previous studies have primarily focused on developing geolocation correction methodologies for full-waveform data at both global and local scales. Global-scale approaches aim to correct systematic errors across diverse regions, whereas local-scale methods refine geolocation accuracy at specific study sites. For instance, Tang et al. (2023) assessed GEDI ground elevation data by comparing it to USGS 3D Elevation Program (3DEP) bare-earth airborne laser scanning (ALS) data. Their waveform co-location analysis focused on evaluating and mitigating global geolocation errors. Notably, only ground returns from 3DEP were used, rather than the full waveform, to minimize discrepancies caused by seasonal variations in canopy structure. Since 3DEP data are predominantly collected during leaf-off conditions, optimal for topographic mapping, this selective approach ensured a more reliable comparison. Global assessments of GEDI Version 001 (Dubayah et al., 2020b) reported mean horizontal geolocation errors exceeding 25 m. Subsequent improvements in Version 002 (Dubayah et al., 2021), released in April 2021, reduced this error to approximately 10 m through enhanced global calibration. While these refinements improved overall accuracy, footprint-level geolocation precision remains subject to localized factors that require targeted correction strategies.

At the local scale, Schleich et al. (2023) employed a high-resolution (1 m) ALS-derived DTM representing ground surface elevations and a photogrammetric digital surface model (DSM) to refine GEDI geolocation accuracy at two forested sites in France. Using a flow accumulation algorithm applied to a mean absolute error map between GEDI ground elevations and a reference DEM, they determined the optimal footprint positions. Their validation revealed mean geolocation errors of approximately 24 m in V001 and 11 m in V002. However, their correction approach proved less effective over flat terrain due to limited topographic variation and challenges in detecting GEDI waveform ground returns.

Similarly, Xu et al. (2023b) proposed a waveform matching approach to evaluate and correct horizontal geolocation errors of GEDI footprints. This method involves simulating waveforms from ALS NEON data using the GEDI simulator and matching these simulated waveforms with GEDI observations. This approach has shown promise in correcting local geolocation offsets, improving the accuracy of GEDI footprint positioning. However, it does not explicitly account for system errors such as laser pointing uncertainties and range errors. Furthermore, seasonal variations in canopy structure were not considered which may affect the shape of the waveform and complicate the geolocation correction process.

Beyond GEDI, Wang et al. (2020) analyzed the geolocation accuracy of the Ice, Cloud, and Land Elevation Satellite/Geoscience Laser Altimeter System (ICESat/GLAS) data using a DSM-based footprint positioning approach in diverse landscapes. Although effective in urban settings with high spatial heterogeneity, this method performed poorly in regions with strong spatial correlation. One limitation stems from DSMs recording only maximum heights per grid cell, failing to capture detailed three-dimensional ground structures. This simplification particularly affects the alignment of the waveforms in forested areas, where the complexity of the canopy and the terrain under the ground influence the accuracy of the geolocation. Additionally, reliance on spectral data from public libraries introduces further uncertainty, as these datasets may not fully represent natural spectral variability.

Developing robust geolocation correction strategies that address these challenges, without relying on costly hardware enhancements, is essential. Such advancements will improve the integration of spaceborne LiDAR with complementary remote sensing datasets, leading to more accurate vegetation and topographic measurements across multiple spatial scales.

1.3. Satellite laser altimetry simulation approaches

Various methods can be used to simulate LiDAR waveforms, including empirical models and radiative transfer (RT) models. To effectively address the geolocation errors in spaceborne LiDAR data, it is crucial to realistically mimic the actual waveforms. A consistent and robust simulation framework that reflects the complexities of real-world conditions is essential. By enhancing the fidelity of waveform simulations, we probably can improve the precision of geolocation corrections.

Empirical models represent the LiDAR waveform as a summation of Gaussian profiles derived from the convolution of target reflectance and pulse energy distribution (Blair and Hofton, 1999; Chauve et al., 2007). For instance, the GEDI simulator (Hancock et al., 2019) is an ALS-basedmodel using the approach outlined in Blair and Hofton (1999), which has been validated across diverse forest types, ALS parameters, and survey configurations. While computationally efficient, these models may lack the accuracy needed for some applications (Wang et al., 2020). Additional geolocation error may also be introduced in the

simulated footprints due to variations in the airborne LiDAR instrument parameters (e.g., wavelength), acquisition parameters (e.g., footprint diameter, point density), and surface conditions (e.g., leaf-off vs. leaf-on).

Radiative transfer models rooted in physical principles can be used to simulate complex light-surface interactions and instrument parameters to generate realistic LiDAR data. The RT model results can also be used to validate and interpret laser altimetry data. Typically, RT models are categorized as forward when rays are traced from the source and backward when traced from the receiver. For instance, forward Monte Carlo (MC)-based LiDAR models include Ray Transfer (RayTran) (Govaerts and Verstraete, 1998) and the Discrete Anisotropic Radiative Transfer (DART) (Gastellu-Etchegorry et al., 2016; Yin et al., 2016). Conversely, backward MC-based LiDAR models include the Digital Imaging and Remote Sensing Image Generation (DIRSIG) (Lach et al., 2006) model. The DART model also supports a bi-directional mode (i.e., combination of forward and backward ray tracing) (Yang et al., 2022).

In addition to Monte Carlo-based models, analytical RT models have been developed for simulating LiDAR waveforms. These models offer advantages in computational efficiency compared to MC-based methods but may sacrifice some level of accuracy, especially in complex vegetation structures. For example, the Geometric Optical-Radiative Transfer (GORT) model (Ni-Meister et al., 2001) integrates geometric optics with radiative transfer to simulate the interaction of light with canopy structures at the forest stand scale. Similarly, the Advanced Canopy Tracing Simulator (ACTS) (Ni-Meister et al., 2010) employs a simplified two-stream radiative transfer approach to account for foliage clumping effects on light propagation through the canopy. While these analytical models are computationally efficient, they may not fully capture the complexity of light interactions in heterogeneous vegetation environments.

The DART model offers a comprehensive RT modeling approach (Gastellu-Etchegorry et al., 1996, 2017), and it has been used extensively in the remote sensing community for a number of applications (Durrieu et al., 2013; Widlowski et al., 2015). The DART-LiDAR module employs a Ray Carlo approach, an accelerated ray-tracking method for simulating multi-platform, multi-type LiDAR system signals, as described in Gastellu-Etchegorry et al. (2016) and Yin et al. (2016). The DART-LiDAR model has been validated with both airborne Land, Vegetation, and Ice Sensor (LVIS) and spaceborne GEDI observations (Yang et al., 2022). Moreover, DART has been extensively used in diverse LiDAR-related research endeavors, including inversion algorithm development (Hmida et al., 2017), satellite sensor design (e.g. CNES LiDAR mission project Durrieu et al. (2013)), and impact assessments of canopy structure and sensor configuration on LiDAR acquisition (Qin et al., 2017; Wei et al., 2020).

1.4. Study objectives

The objective of our study is to assess and improve the geolocation accuracy of a full-waveform spaceborne LiDAR system across different canopy types. To our knowledge, no prior research has fully utilized the complete waveform, integrating both terrain and vegetation signals through a radiative transfer (RT) physical model like DART. This approach captures the interactions and replicates actual waveforms for footprint-level geolocation corrections in complex forest environments, while accounting for spaceborne LiDAR geometry and instrument configuration.

Our method employs a comprehensive approach to reconstruct realistic 3D vegetation scenes from dense, multi-directional ALS data collected by the Goddard LiDAR, Hyperspectral, and Thermal Imager (G-LiHT) instrument. Additionally, we use a physics-based RT model to simulate the interactions between the 3D forest representation and laser pulses, thereby enhancing the fidelity of our simulations across different forest structures.

The specific objectives of this study are: (i) to assess the random geolocation accuracy of individual GEDI footprints, (ii) to determine the systematic geolocation accuracy across GEDI tracks, and (iii) to investigate how canopy type influences the quality of geolocation corrections.

2. Study sites

We selected three research sites that include a small variety of forest structural and compositional characteristics that account for key variation in the ability to match simulated data with its spaceborne counterpart (Fig. 1). The first site is a closed canopy deciduous forest located at the Smithsonian Environmental Research Center (SERC) in Edgewater, Maryland (38°53′33″N, 76°33′37″W), covering an area of 36 ha (600 × 600 m). SERC serves as a terrestrial National Ecological Observatory Network (NEON) site and features a mixed-species mature deciduous forest where American sweetgum (*Liquidambar styraciflua*) and tulip poplar tree (*Liriodendron tulipifera*) dominate the over-story. Other common species include Mockernut hickory (*Carya tomentosa*), white oak (*Quercus alba*), red oak (*Quercu rubra*) and American beech (*Fagus grandifolia*), with ironwood (*Carpinus caroliniana*) and various small tree species forming a dense under-story (Kamoske et al., 2019).

The second site is a closed canopy coniferous forest at the closed canopy conifer (Howland) Research Forest (45°12′21.744″N, 68°44′33.54″W), covering an area of 100 ha (1000 × 1000 m). The Howland Research Forest, owned by the Northeast Wilderness Trust, serves as a dedicated research area for exploring forest ecosystems in central Maine. The valley constitutes a mature transitional conifer forest characterized by flat to gently rolling terrain, with a maximum relief of less than 68 m within a 10 km area (Sihi et al., 2018). Red spruce (*Picea rubens Sarg.*) and eastern hemlock (*Tsuga canadensis (L.) Carr.*) stand out as the dominant tree species, accompanied by a mix of associated hardwoods. A two-lane paved road crosses the eastern portion of the site with a roughly N-S orientation.

The third site is an open canopy coniferous forest at the Gus Pearson Natural Area near Flagstaff, AZ (35°16′23″N, 111°44′40″W), covering an area of 16 ha (400 × 400 m). This site is characterized by the heterogeneity of its forest canopy and gaps. The vegetation fractional cover at this site is around 50%, and is predominantly composed of Ponderosa Pine (Pinus ponderosa) (Biondi, 1996). A paved, two-lane road crosses the site with NNW-SSE orientation, with a notable break in the canopy.

For the rest of this paper, we will refer to each site by its respective canopy type, closed canopy deciduous (SERC), closed canopy conifer (Howland), and open canopy conifer (Gus Pearson), rather than by the site name. This classification will facilitate clearer interpretation and comparison of results across different forest structures.

3. Data

3.1. G-LiHT airborne laser scanning data

Airborne LiDAR campaigns were performed for each site with NASA Goddard's LiDAR, Hyperspectral, and Thermal Imager (G-LiHT) using a 1550-nm airborne laser measurement system. Acquisition dates were July 2021 for closed canopy deciduous (SERC) using the v2 instrument (Riegl VQ 480i), June 2012 for closed canopy conifer (Howland), and March 2013 for Gus Person, both using the v1 instrument (Riegl VQ-480).

The dense, multi-directional flight plans generated ALS datasets with a broad range of scan angles (±30°), an 11–12 cm diameter laser footprint, and point densities of approximately, 55 m^{-2}, 40 m^{-2}, and 22 m^{-2} for the three sites, respectively. We used the 1 m posting DTM and CHM products distributed by G-LiHT for each site (Fig. 1). Additional details regarding the G-LiHT data acquisition and other metrics are detailed in Yin et al. (2022).

Table 1
Metadata for filtered GEDI products analyzed at each study site.

Study site	Closed canopy deciduous (SERC)		Closed canopy conifer (Howland)		Open canopy conifer (Gus Pearson)	
G-LiHT Acquisition date	July 28, 2021		June 21, 2012		March 31, 2013	
GEDI Acquisition date	May 8, 2019	May 2, 2022	June 4, 2019	June 4, 2019	May 7, 2022	May 9, 2022
Number of footprints (M)	13	5	4	20	7	5
Orbit ID	02273	19178	02704	02704	19256	19282
Beam number	1011	0001	0101	0110	1011	0110
Degradation flag	0	0	0	0	0	0
Quality flag	1	1	1	1	1	1
Sensitivity	>0.97	>0.95	>0.97	>0.97	>0.95	>0.95

3.2. GEDI satellite laser altimetry data

We identified Level-1B and Level-2B GEDI waveform products for each site with acquisition dates corresponding to the collection season of the G-LiHT data. As recommended in Dubayah et al. (2021), we only included high-quality footprints (i.e., quality_flag = 1), with good waveform quality and without potential for degraded geolocation under sub-optimal operating conditions (i.e., degrade_flag = 0). Each Level-2B GEDI shot includes a sensitivity value, representing the estimated maximum canopy cover penetration given the signal-to-noise ratio of the waveform. We selected waveforms with sensitivity values greater than 0.95. Table 1 summarizes the relevant GEDI metadata for the three study sites.

These filters reduced the available GEDI data for our study sites. For example, only 6 of 20 possible GEDI granules were acquired during the leaf-on season (May-August) at the closed canopy deciduous (SERC) site. Subsequent quality and sensitivity filters further refined the SERC selection to only two granules, with a total of 18 footprints from two beams (13 from beam "1011" in Orbit #02273 and 5 from beam "0001" in Orbit #19256) intersecting the study area.

We assume that the mature, closed-canopy deciduous forest at SERC exhibits minimal structural changes over short periods (1–2 years). Additionally, both GEDI and ALS acquisitions were conducted under similar leaf-on conditions, reducing potential discrepancies due to phenological variations. Since leaves are the primary scattering surfaces, seasonal differences typically introduce greater variability than interannual variations within the same season. At Howland and Gus Pearson, coniferous forests exhibit slow growth rates and structural stability. Long-term studies on biomass accumulation and canopy height at Howland confirm minimal structural changes over these periods (Hollinger et al., 2021).

4. Methods

Our workflow, depicted in Fig. 2, highlights the key methods, models, inputs, and products of this study. Initially, we reconstruct a 3D scene using ALS point cloud data. Subsequently, we simulate GEDI waveforms using DART, enabling a comparison of these waveforms to estimate geolocation offsets.

4.1. Realistic 3D scene reconstruction

To reconstruct the forest scenes, we used the PVlad model, a physically-based approach outlined in Yin et al. (2022). This model leverages the apparent reflectance of the ALS point cloud to estimate plant area index (PAI) and voxel-based plant area density (PAD). The goal is to reduce reliance on additional field measurements, such as gap probability. The PVlad concept integrates information from multi-directional ALS scans, quantifying the interception percentage of each voxel for classification and occlusion correction. This integration facilitates the development of rigorous volumetric sampling methods to derive PAI and PAD. The model was validated during both leaf-on and leaf-off seasons at the closed-canopy deciduous (SERC) (Regaieg et al., 2021; Yin et al., 2022). A voxel size sensitivity analysis was conducted using voxel sizes of 0.5 m, 1.0 m, 2.0 m, and 5.0 m. The estimates of LAI and LAD captured structural differences between mature, logged, and intermediate-aged stands over eight forest plots. LAI values were validated against field litter collection measurements, while the vertical LAD distribution was compared to the output of the VoxLAD model using terrestrial laser scan (TLS) field survey data (Béland and Baldocchi, 2021). The results demonstrated a strong correlation ($R \approx 0.9$), with RMSE < 0.5 for LAI (for 1 and 2 m voxel sizes) and $RMSE \approx 0.028$ for vertical LAD (for 0.5 and 1 m voxel sizes). Additionally, upper-canopy LAD exhibited low variance for voxel sizes $\leq$2 m across all forest stands.

In this study, the PVlad model was applied to the G-LiHT data, using voxel dimensions of 0.5 m for closed canopy deciduous (SERC) and open canopy conifer (Gus Pearson), and 1.0 m for closed canopy conifer (Howland). A 1 m voxel size was used to efficiently allocate computational and memory resources for the larger domain and dense vegetation at the closed canopy conifer (Howland) site. We adopted the 0.5 m voxel size for PAD estimation to ensure consistency with prior studies while maintaining fine-resolution structural information. The resulting PAI maps document the higher density of the Howland and closed canopy deciduous (SERC) sites compared to open canopy conifer (Gus Pearson) (Fig. 1).

The reconstructed forest scenes (SERC and Gus Pearson) in Yin et al. (2023) demonstrate the high fidelity of the PVlad model in generating realistic forest structures. These scenes were used to simulate very-high-resolution (VHR) optical imagery and derive DSMs using stereophotogrammetry. Comparisons with DSMs derived from WorldView satellite imagery showed that the simulated DSMs closely matched the WorldView DSMs, with vertical bias of less than 1.6 m and RMSE values below 1 m. As illustrated in Fig. 2, the DART-DAO (Data Access Object) module (Regaieg et al., 2021) was used to reconstruct realistic 3D scenes from the PVlad output and the 1 m G-LiHT DTM. The resulting scene serves as input to the DART model used to simulate GEDI waveforms.

4.2. Waveform simulation

In DART, parameters are categorized into two main types: geometric and radiative. Geometric parameters define the characteristics of the virtual GEDI instrument, including wavelength, pulse energy, sampling rate, and sensor viewing geometry. The laser pointing direction is determined using zenith and azimuth unit vectors from the GEDI L1B product ("`local_beam_azimuth`" and "`local_beam_elevation`"), representing the laser orientation in the local East-North-Up (ENU) frame. Radiative parameters describing scene optical properties are defined in DART using site-specific inputs. Leaf optical properties are derived from field-measured biochemical data (Regaieg et al., 2021) for SERC, or for other sites, assigned based on vegetation type (coniferous, deciduous) from spectral databases available in DART. Ground reflectance is defined using a representative soil spectrum from the JPL Spectral Library[1] (e.g., Alfisol: loam-gravelly dark brown soil for the SERC site). To ensure consistency with GEDI observations, we applied the GEDI L2B canopy-to-ground backscattering ratio (1.5:1) as an empirical scaling factor, aligning simulated radiative transfer with

[1] http://speclib.jpl.nasa.gov/.

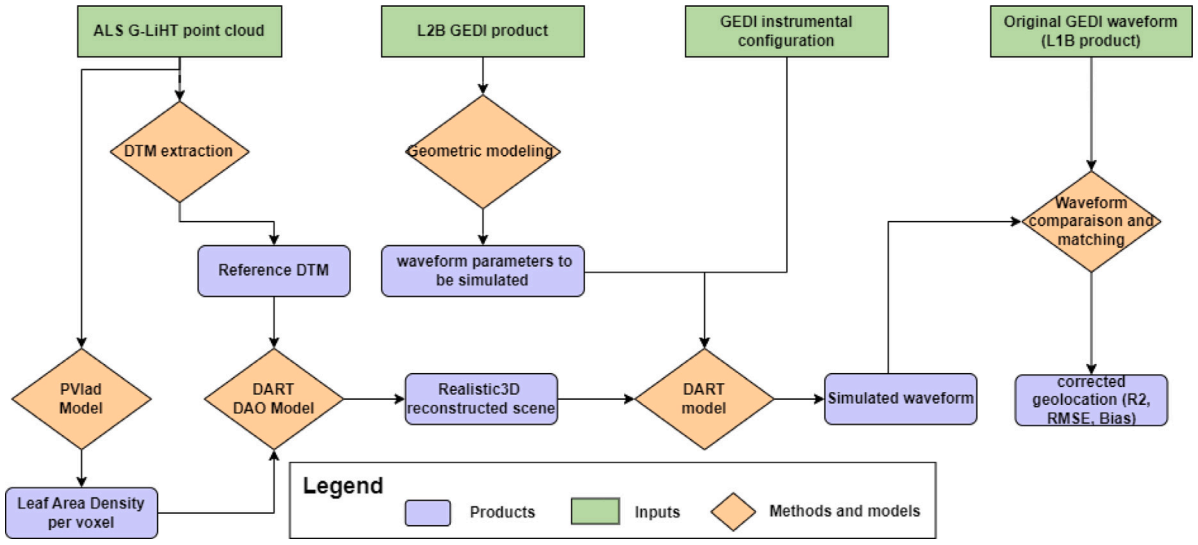

Fig. 2. Flowchart of data preparation, simulation and waveform matching workflow for GEDI geolocation refinement.

GEDI characteristics without implying equivalence between reflectance and backscattering coefficients.

We used DART to simulate GEDI waveforms at multiple locations within a search area surrounding each original GEDI L1B footprint position. The search area was defined as a 50 × 50 m grid with a step size of 1 m, resulting in $N = 2601$ unique positions for simulated waveforms (Figure S1). The 1 m step size captures the spatial variability of waveforms without oversampling, and the 50 m search window spans the estimated 10 m geolocation error of the GEDI V002 data products.

4.3. Waveform processing

First, we removed the mean EGM96 geoid height offset from the G-LiHT data for each site, ensuring all comparisons utilized the vertical datum of the GEDI data, with elevation values expressed in meters above the WGS84 Ellipsoid. Next, we subtracted the mean background noise value (Level-1B GEDI product: " `noise_mean_corrected`") from the observed GEDI waveform amplitude. We applied a Gaussian filter with a width of 20 ns to the observed GEDI waveform to reduce residual random background noise. To ensure consistent processing, the same filter was applied to each simulated waveform. This filtering step primarily smooths background noise while preserving the waveform pattern associated with vegetation structure. Finally, we normalized the amplitude of each simulated waveform ($\hat{A}(t)$) to match that of the observed GEDI waveform amplitude ($A(t)$). The normalization factor α was computed as the ratio of the mean observed to the mean simulated waveform amplitude:

$$\alpha = \frac{\overline{A}(t)}{\overline{\hat{A}}(t)} \tag{1}$$

and used to compute the normalized simulated waveform amplitude $\alpha\hat{A}_{i,j}$.

To evaluate the accuracy of the simulated waveforms, we computed the Root Mean Square Error (RMSE) between the observed and normalized simulated waveform at each position (i, j) within the search area (i and j $\in [-25, 25]$):

$$\mathrm{RMSE}_{i,j} = \sqrt{\frac{1}{n}\sum_{t=1}^{n}\left(A(t) - \alpha\hat{A}_{i,j}(t)\right)^2} \tag{2}$$

where n represents the total number of discrete time bins in each waveform.

To assess the similarity between the observed and simulated waveforms, we computed a coefficient of correlation (determination), $r^2(i, j)$ for the simulated waveform at each position. We propose that the position with the highest correlation coefficient indicates the best match between the observed and simulated waveforms, corresponding to the actual geolocation of the GEDI measurement. Higher values reflect greater alignment in shape and amplitude, suggesting similar forest structures.

$$r^2_{i,j} = \left(\frac{\mathrm{cov}(A, \alpha\hat{A}_{i,j})}{\sigma_A \cdot \sigma_{\alpha\hat{A}_{i,j}}}\right)^2 \tag{3}$$

where cov is the covariance of the two waveform amplitudes, and σ is the standard deviation of each waveform amplitude. The $r^2_{i,j}$ values measure the proportion of the variance between the observed and the simulated waveforms regardless of the scalar α, as r^2 is invariant under scaling of the dependent variable $\hat{A}(t)$.

By identifying the location (i,j) with the maximum value, we can infer the most accurate geolocation for the recorded GEDI waveform. The geolocation offset for each footprint is thus determined from this maximum correlation value within the search domain.

$$dx, dy = \arg\max\left(\{r^2_{i,j}\}\right) \tag{4}$$

To ensure that waveform matching accurately reflects both overall correlation and the spatial alignment of the ground elevation values, an additional condition was introduced. In dense vegetation, waveform similarities can sometimes result in high correlation, even when the geolocation is incorrect. To address this, we impose a constraint that evaluates the alignment of ground elevation values between the simulated and GEDI waveforms. Specifically, a 1.5 m distance threshold is applied to measure the offset between the observed and simulated ground elevation values. If the offset exceeds this threshold, a penalty is applied. This threshold was carefully chosen to balance accuracy and data retention, taking into account the expected precision of waveform-derived ground elevation values. A more lenient threshold (e.g., 2–3 m) could allow misalignments that introduce geolocation errors, while a stricter threshold could result in unnecessary data exclusion.

Finally, we computed the directional components and total magnitude of systematic geolocation error $(\Delta x, \Delta y, \Delta total)$ for each GEDI ground track as the geometric mean and median of the (dx, dy) offsets for all footprints in the track. We computed random geolocation error $(\sigma_{dx}, \sigma_{dy}, \sigma_{total})$ as the standard deviation and normalized median absolute deviation (NMAD, the robust equivalent of standard deviation, less susceptible to outliers) of the (dx, dy) offsets.

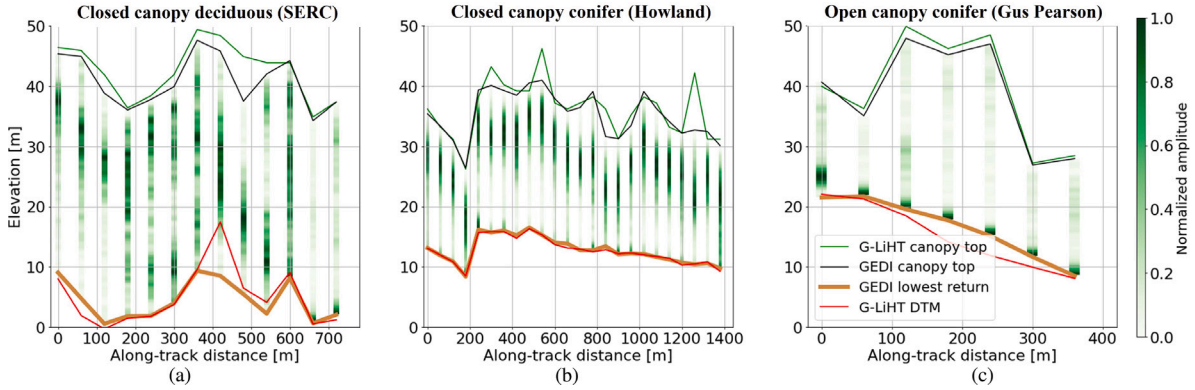

Fig. 3. GEDI Level-1B waveform and Level-2B derived canopy top and lowest mode (ground surface) elevation values for the three study sites. (a) closed canopy deciduous (SERC orbit #02273), (b) closed canopy conifer (Howland #02704) where the first 4 waveforms from beam 0101 and the remaining waveforms from beam 0110, and (c) open canopy conifer (Gus Pearson #19256) sites. Darker green values indicate higher normalized amplitude values, representing a denser canopy. The red and green curves show the mean of the 1 m G-LiHT DTM and canopy top raster values within each 25 m GEDI footprint, respectively.

Table 2
Metrics from linear models quantifying elevation differences between the spaceborne GEDI Level-2B and reference airborne G-LiHT for two surfaces (top-of-canopy and ground) at the three study sites. Model relationships reflect temporal offsets between acquisitions and initial GEDI geolocation errors and other factors.

Site	Top-of-canopy			Ground		
	Bias [m]	RMSE [m]	r^2	Bias [m]	RMSE [m]	r^2
Closed canopy deciduous (SERC)	1.69	2.46	0.90	0.50	2.72	0.85
Closed canopy conifer (Howland)	0.93	2.61	0.83	−0.13	0.30	0.99
Open canopy conifer (Gus Pearson)	0.82	1.16	0.98	−1.47	2.0	0.96

4.4. Comparison of DART and GEDI simulator waveforms

To further evaluate the DART waveform results, we used the GEDI Simulator (Hancock et al., 2019) to simulate GEDI waveforms directly from the G-LiHT point cloud data using the same observation geometry and instrument configuration as the DART simulations. We applied the same waveform normalization approach and computed the same metrics for the GEDI Simulator waveforms.

We then performed the following comparisons between: (i) the observed GEDI waveforms and those generated by the GEDI Simulator, to investigate how well it replicated real-world observations for our study sites, (ii) the best-matched waveforms from both simulated datasets, and (iii) the corresponding geolocation offset (dx, dy) for the best-matched waveforms.

5. Results

In this study, we aim to evaluate the accuracy of simulated GEDI waveforms and their potential for refining geolocation accuracy. To quantify forest structure using both G-LiHT and GEDI elevations, Table 2 compares GEDI Level-2B estimates with reference G-LiHT-derived top of canopy (TOC) height and ground elevation across the three study sites. At the closed-canopy conifer site (Howland), ground elevation values exhibit strong agreement ($r^2 = 0.99$) with minimal bias and RMSE. In contrast, larger discrepancies are observed at the closed-canopy deciduous site (SERC) and the open-canopy conifer site (Gus Pearson), likely due to more complex terrain at these locations (Fig. 1).

Despite the temporal offset between some G-LiHT and GEDI acquisitions, the observed error and correlation values suggest sufficient agreement for subsequent waveform comparisons.

5.1. Waveform comparison over the closed canopy deciduous site

By comparing waveforms at the original GEDI footprint positions and the best-matched simulated positions at the closed-canopy deciduous site (Fig. 4), we assess the alignment between observed and simulated waveforms and the fidelity of DART simulations in capturing fine-scale waveform variations. The results show discrepancies between the observed and simulated waveforms at the original GEDI positions, suggesting a spatial shift in alignment. However, the best-matched simulated waveforms exhibit improved agreement with the observed GEDI waveform, effectively capturing small-scale variations despite the complexity of the multi-layered canopy.

The correlation maps (Fig. 5) illustrate the spatial distribution of correlation scores between observed and simulated waveforms across 2601 tested positions. Each map exhibits one or more correlation peaks, indicating locations where simulated waveforms best match the observed GEDI waveform. Some footprints (e.g., F1 and F3) display a broad distribution of high correlation values, likely due to structural similarities within the vegetation and terrain. In contrast, footprints with more localized correlation peaks (e.g., F7, F12, F13) suggest a more distinct best-match position. The relative direction and magnitude of the derived footprint offsets for the 13 best-matched waveforms are variable within the same ground track.

To further examine the influence of canopy structure on waveform matching, Fig. 6 presents a detailed comparison of two sample footprints, one over a homogeneous closed canopy and another over a heterogeneous canopy with gaps. In the homogeneous closed canopy (F3), the similarity among simulated waveforms results in a broader distribution of high correlation values. Conversely, in heterogeneous canopy with gaps (F13), distinct waveform differences lead to a sharper correlation peak, allowing for a more precise determination of the best-matched position.

Fig. 7 quantifies the improvement in waveform agreement at the best-matched positions. Compared to the original GEDI positions, the best-matched waveforms show an increase in correlation coefficient (r^2) values from $[0.52, 0.92]$ to $[0.91, 0.97]$ and a decrease in RMSE values from $[0.35, 0.77]$ to $[0.18, 0.58]$, indicating a higher level of agreement with the observed GEDI waveform.

Results for the second ground track at this site are shown in Figures S2–S3.

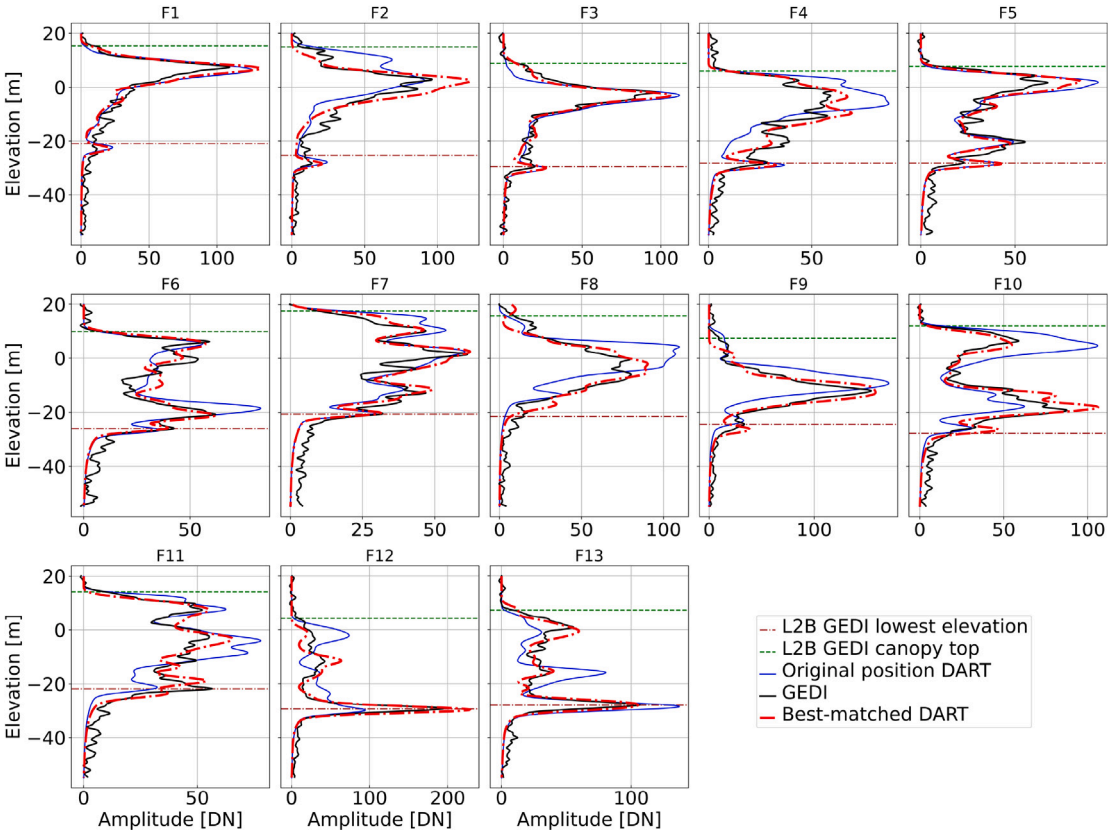

Fig. 4. Comparisons between the observed Level-1B and DART-simulated GEDI waveforms for orbit #02273 over the closed canopy deciduous (SERC) site. The black curve is the observed GEDI waveform, the blue curve is to the simulated waveform at the original GEDI position, and the red curve is the best-matched simulated waveform within the search area. Note improved agreement of the best-matched simulated waveforms with the observed GEDI waveform for all footprints.

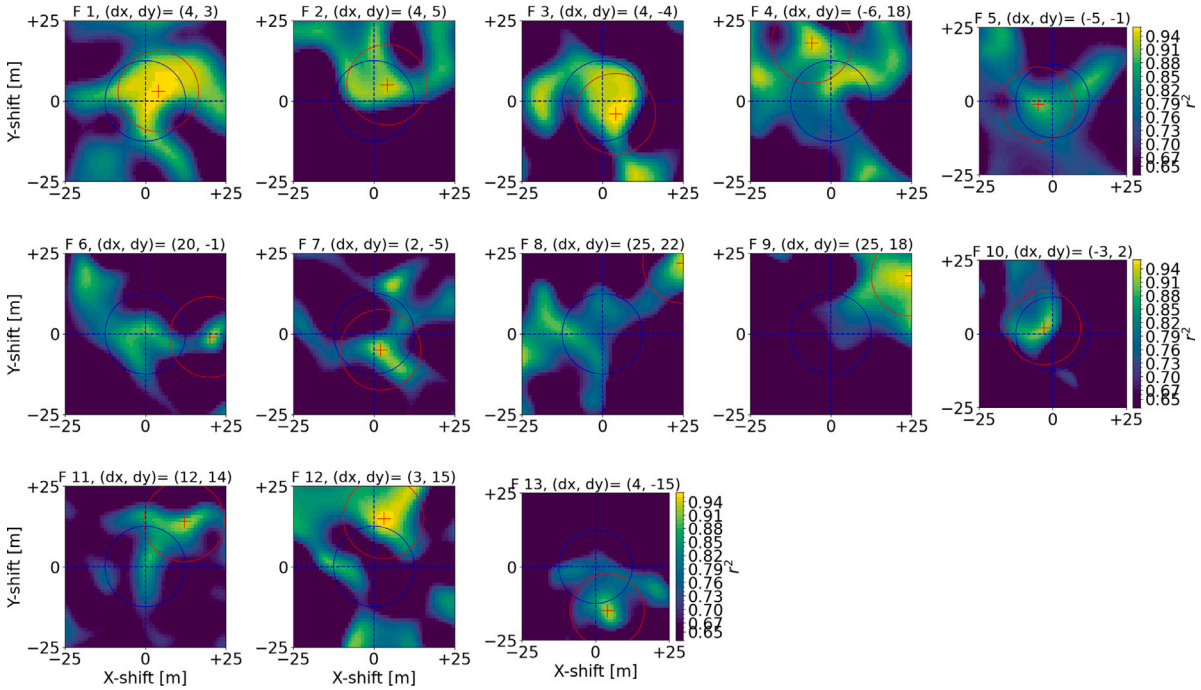

Fig. 5. Maps of correlation score between original and DART simulated GEDI waveforms for the closed canopy deciduous (SERC) site: dashed lines intersecting at (0,0) show the original GEDI footprint position, the blue circle is to the original GEDI footprint with 25 m diameter, and the red cross and red circle show the relative position of the best-matched simulated waveform (peak correlation value), with corresponding dx and dy offset values in the title.

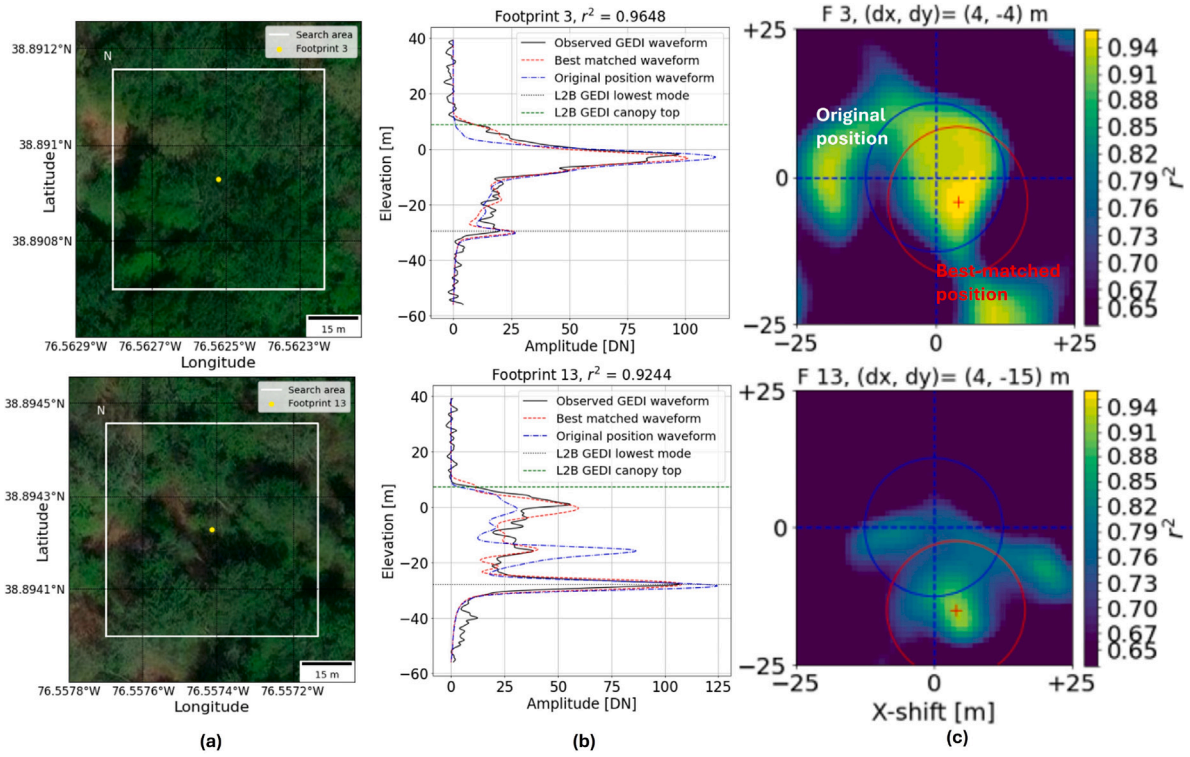

Fig. 6. Comparison between sample GEDI footprints over homogeneous (top row) and heterogeneous (bottom row) canopy at the closed canopy deciduous (SERC) site. (a) ESRI World Imagery basemap centered on the original GEDI footprint location, with white square indicating the 50 m search area, (b) the corresponding waveforms, and (c) the corresponding correlation maps. See figure captions above for details. Canopy heterogeneity improves correlation peak identification and confidence in the resulting best-matched waveform position.

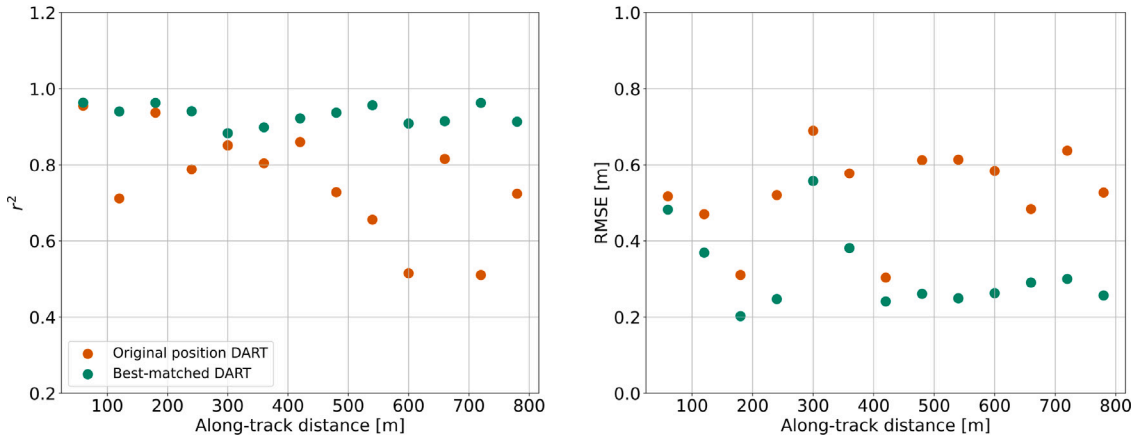

Fig. 7. Correlation coefficient and RMSE values for the simulated waveforms at the original and best-matched positions for all footprints in orbit #02273 over the closed canopy deciduous (SERC) site. Note improvement in both metrics for the best-matched waveforms.

5.2. Waveform comparison over the closed canopy conifer site

To compare the waveforms and correlation scores for the closed canopy conifer site, Fig. 8 shows two sample footprints. The top row depicts footprint F21, which intersects a homogeneous canopy with an open road, while the bottom row illustrates footprint F6, representing a dense, closed, homogeneous canopy. Both the observed and simulated waveforms appear simpler than those for the closed canopy deciduous (SERC) site, due to dominance of the upper layer of coniferous forest. While the normalized simulated waveforms show better agreement with observed amplitude at the closed canopy conifer, many footprints (e.g., F6 in Figure S5 and 8) have a broader distribution of high correlation values and less distinct peaks. This can be attributed to the similarity in canopy structure (e.g., dense, closed, homogeneous canopy), which complicates identification of the best-matched waveform position and corresponding geolocation offset. However,

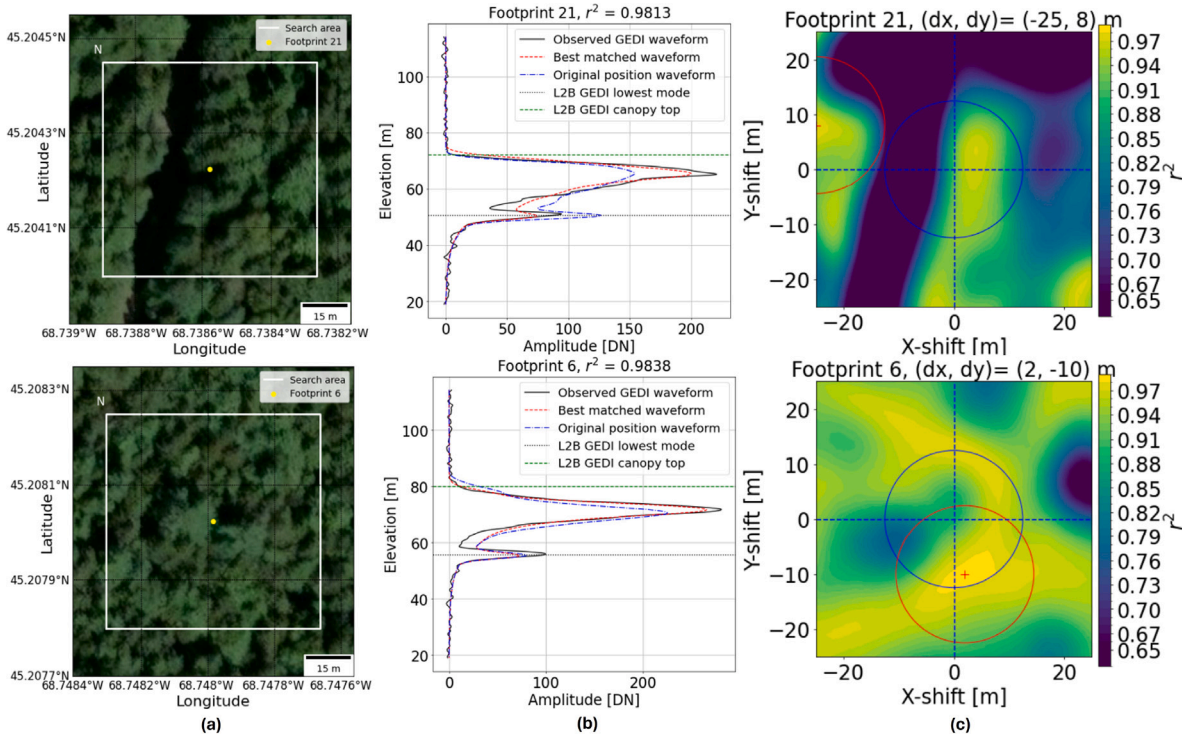

Fig. 8. Two sample GEDI footprints over different types of coniferous canopy at the closed canopy conifer (Howland) site. The top row shows F21, depicting a homogeneous canopy intersected by an open road. In contrast, the bottom row (F6) shows results for a dense, closed and homogeneous canopy. See Fig. 1 for context and Fig. 6 caption for additional details.

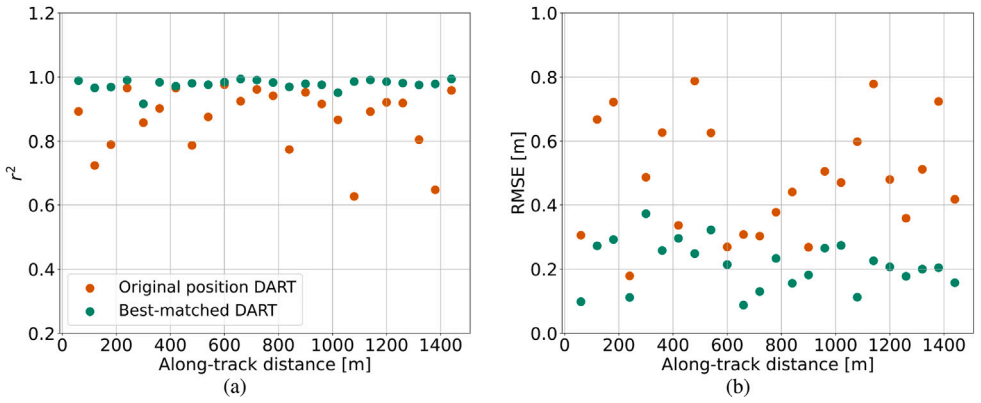

Fig. 9. Correlation coefficients and RMSE values for comparisons between the observed and simulated waveforms at the original and best-matched positions for all GEDI footprints in orbit #02704 over the closed canopy conifer site (Howland). Note improvement in both metrics for the best-matched footprint locations.

footprints over search areas with more variability, including roads and gaps between trees (e.g., F21) should have improved final geolocation position confidence.

Correlation coefficients for closed canopy conifer (Howland) increased from $[0.67, 0.97]$ to $[0.95, 0.99]$ and RMSE values decreased from $[0.18, 0.91]$ to $[0.09, 0.38]$, indicating improved alignment between the observed and best-matched simulated waveforms (Fig. 9).

5.3. Waveform comparison over the open canopy conifer site

Sample footprints for the open canopy conifer site are shown in Fig. 10, with all 7 footprints shown in Figures S6–S7.

We observe agreement between the observed and best-matched waveforms, with strong ground returns. The heterogeneity of the canopy at this site leads to tighter correlation value peaks, which improves confidence in the final best-matched simulated waveform position compared to sites with more homogeneous canopy.

Correlation coefficients increased from $[0.78, 0.94]$ to $[0.93, 0.95]$ and RMSE decreased from $[0.21, 0.76]$ to $[0.19, 0.58]$ (Fig. 11). Results for the second ground track (orbit #19282) show similar improvements (Figures S8–S9).

5.4. Systematic and random geolocation error

To analyze the geolocation errors across the study sites, closed canopy deciduous, closed canopy conifer, and open canopy conifer, we differentiate between systematic errors, which represent consistent offsets in geolocation, and random errors, which capture the variability in geolocation positions across the footprints. The geolocation offsets for all footprints along the GEDI ground tracks over these sites are presented in Fig. 12, with summary statistics provided in Table 3.

We observe a variable systematic offset magnitude and direction across the three sites. These observed values are within the 10 m geolocation error specification for the L1B GEDI products, except for

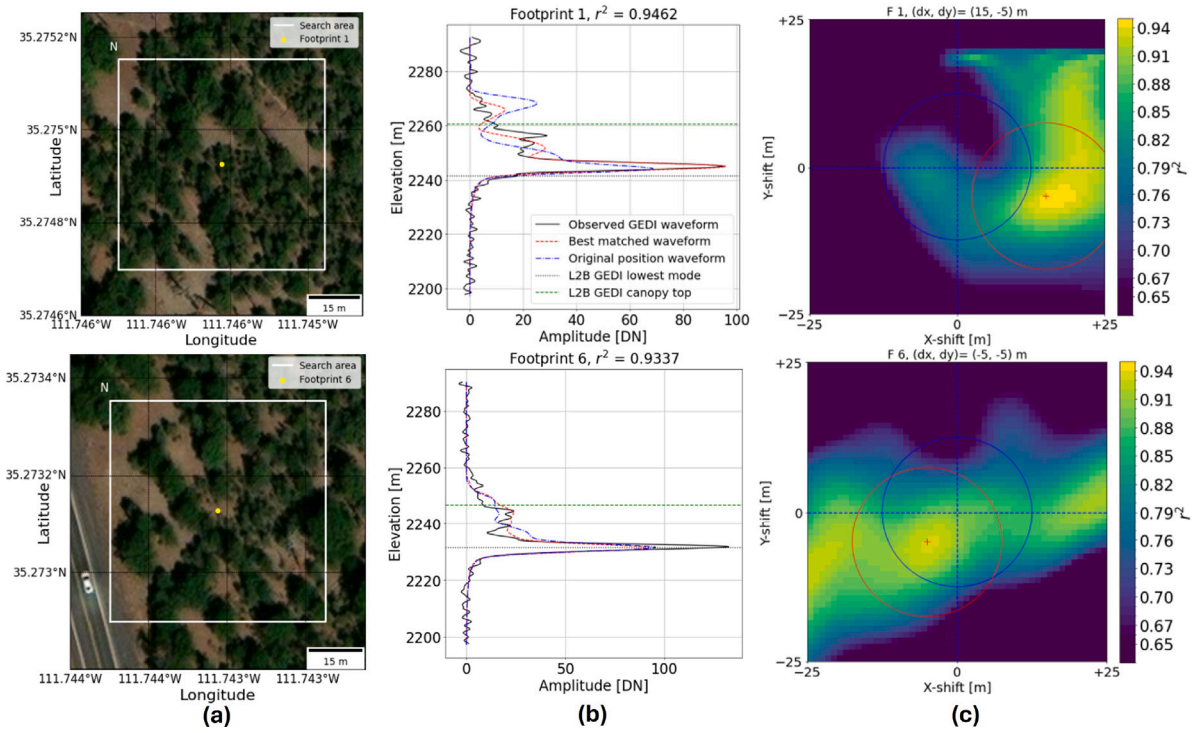

Fig. 10. Two sample GEDI footprints from orbit #19256 over heterogeneous and open canopy at the open canopy conifer (Gus Pearson) site. The top and bottom rows show F1 and F6, respectively. See Fig. 1 for context and Fig. 6 caption for additional details.

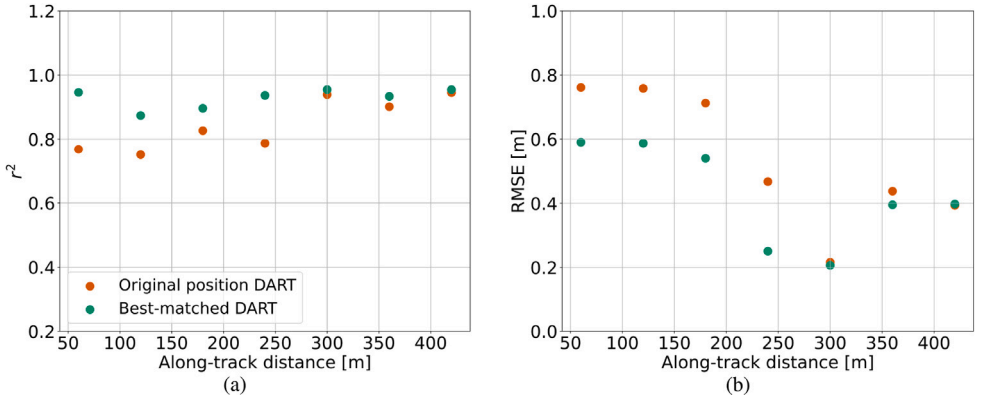

Fig. 11. Correlation coefficients and RMSE values for comparisons between the observed and simulated waveforms at the original and best-matched positions for all footprints in orbit #19256 for the open canopy conifer (Gus Pearson). Note improvement in both metrics for the best-matched footprint locations.

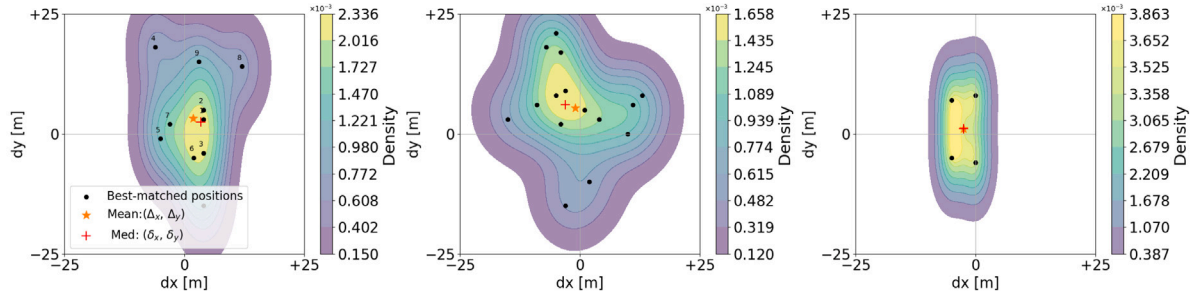

Fig. 12. Best-matched waveform positions (dx, dy) for the selected footprints at each site (black dots with annotation for corresponding footprint numbers). The orange star shows the mean offset (Δx, Δy) and the red cross shows the median offset for all footprints in the ground track. Color ramp shows point density (pt/m^2). (For interpretation of the references to color in this figure legend, the reader is referred to the web version of this article.)

Table 3
Systematic and random GEDI geolocation errors for the three study sites.

Study site	Orbit ID	Beam number	Systematic Error (m) ($\Delta x, \Delta y, \Delta total$)	Random Error (m) ($\sigma_{dx}, \sigma_{dy}, \sigma_{total}$)
Closed canopy deciduous	02273	1011	Mean: (1.77, 1.88, 9.34) Med: (4.00, 2.00, 5.65)	Std Dev: (5.30, 8.39, 5.97) NMAD: (2.96, 8.89, 1.10)
Closed canopy conifer	02704	0110	Mean: (0.07, 5.57, 11.85) Med: (−3.00, 6.00, 10.50)	Std Dev: (6.76, 9.49, 5.15) NMAD: (5.93, 5.18, 7.07)
		0101	Mean: (15.5, 16.5, 22.3) Med: (15.00, 16.00, 22.30)	Std Dev: (1.50.00, 1.04) NMAD: (2.22, 0.00, 1.45)
Open canopy conifer	19256	1011	Mean: (−2.5, 1.00, 7.41) Med: (−2.5, 1.00, 7.53)	Std Dev: (2.50, 6.15, 0.98) NMAD: (3.70, 9.63, 1.13)

beam 0101 at closed canopy conifer (Howland). This discrepancy can be attributed to the limited number of waveforms available (only 4 waveforms), which may introduce bias. The residual random errors are 2–10 m for the three sites, which captures additional intra-track geolocation errors, and any waveform matching error.

5.5. Comparison with GEDI simulator results

To evaluate the performance of the DART and GEDI simulators in simulating the GEDI waveforms (Fig. 13), we compared the observed waveforms with those generated by each simulator at the deciduous closed canopy site. The waveforms are assessed for their overall similarity, as well as the degree to which they align with the observed GEDI data. All waveform panels are shown in Figures S10–S11

In general, both simulators produced waveforms that appear similar to the observed GEDI waveforms. However, visual inspection, along with the correlation and RMSE values (Fig. 14), reveals that the best-matched simulated waveforms using DART exhibit superior agreement with the observed waveforms compared to those generated by the GEDI simulator.

While both models aim to match the observed GEDI waveform, we notice that same or different matching results can lead to varying dx and dy shifts in waveform alignment. Fig. 15 shows the distribution of (dx, dy) offsets from the best-matched GEDI simulator waveforms over closed canopy deciduous (SERC) with mean of $(-2.11, 6.56)$ and median of $(-3.00, 8.00)$. These values are different from the (dx, dy) offsets for the best-matched DART waveforms (Table 3). While the best-matched positions for some footprints show agreement (e.g., F2, F11), others differ by 10 s of meters, and both datasets contain outliers, likely due to low-confidence matches (e.g., F8). While sample size is limited, the higher correlation scores and lower RMSE values suggest that the positions from the best-matched DART waveforms are closer to the true footprint positions.

To further evaluate the calculated (dx, dy) offsets, we sampled the ground truth G-LiHT TOC and DTM rasters at the best-matched waveform positions for the DART and GEDI simulator results (Fig. 16). The best-matched waveform positions from both simulations show improved alignment of the GEDI Level-2B highest and lowest returns with the mean G-liHT TOC and ground elevations values. The DART positions offer the lowest TOC and ground elevation RMSE values.

6. Discussion

The advances highlighted in this study support space-borne data fusion by enabling the precise integration of vertical structure profiles from LiDAR with horizontal structures of vegetation canopies and surface topography. This combination is crucial for refining 3D models of Earth's surface and vegetation, enhancing the accuracy of data products derived from satellite-based observations.

Table 4
Statistical comparison of waveform shape similarity across voxel sizes, using 0.5 m voxel as the reference.

Voxel size (m)	Bias	RMSE	R^2
1.0	0.00	0.01	0.99
2.0	0.00	0.02	0.96
5.0	0.01	0.09	0.49

6.1. Influence of scene reconstruction on waveform shape

6.1.1. Influence of voxel size

To assess the impact of voxel size on waveform simulation fidelity for GEDI 25 m footprint diameter, we tested voxel resolutions of 0.5 m, 1.0 m, 2.0 m, and 5.0 m (Figure S12), and performed a statistical comparison of waveform shapes derived from these voxel sizes (Table 4). The simulated waveforms corresponding to 0.5 m and 1.0 m voxel resolutions exhibit very similar shapes, indicating that fine structural details of the canopy within the 25 m GEDI footprint are well preserved at these finer scales. In contrast, as voxel size increases to 2.0 m and 5.0 m, noticeable deviations appear in the waveform structure. Specifically, the waveform simulated with a 5.0 m voxel resolution shows a diminished top-of-canopy return and a more pronounced, broader ground return. These differences are likely the result of spatial averaging introduced by larger voxels, which smooth out fine-scale vertical variations and reduce the vertical heterogeneity captured in the vegetation canopy within the GEDI footprint. In addition, larger voxels can induce non-negligible clumping of vegetation within each voxel. This clumping effect leads to unrealistically long interception paths, further distorting the returned waveform and diminishing its ability to represent true canopy structure. Consequently, energy reflected from the canopy is underestimated, while the ground return becomes more dominant due to increased contributions from open gaps within the coarser voxel volume. The statistical comparison (Table 4) further confirms that waveform shape similarity with the baseline (0.5 m voxel) decreases with increasing voxel size. Both bias and RMSE increase with coarser resolutions, and the coefficient of determination (R2) decreases, indicating reduced fidelity to the reference waveform. Based on these observations, the 5.0 m voxel size is deemed too coarse for our geolocation correction approach with the GEDI 25 m footprint, as it significantly alters waveform patterns. We conclude that voxel sizes of 0.5 m or 1.0 m are more appropriate to ensure accurate waveform shapes necessary for reliable geolocation correction of GEDI data.

6.1.2. Influence of Plant Area Density (PAD) estimation uncertainties

To quantify the impact of Plant Area Density (PAD) estimation uncertainty on waveform simulation, we introduced Gaussian noise perturbations of ±10% and ±20% to the voxel-level PAD values, systematically examining both under- and overestimation scenarios. Remarkably, no discernible differences were observed in the resulting waveform shapes across all perturbation levels. The waveform shape is preserved across all scenarios. This insensitivity to PAD estimation errors suggests that the waveform shape and geolocation correction

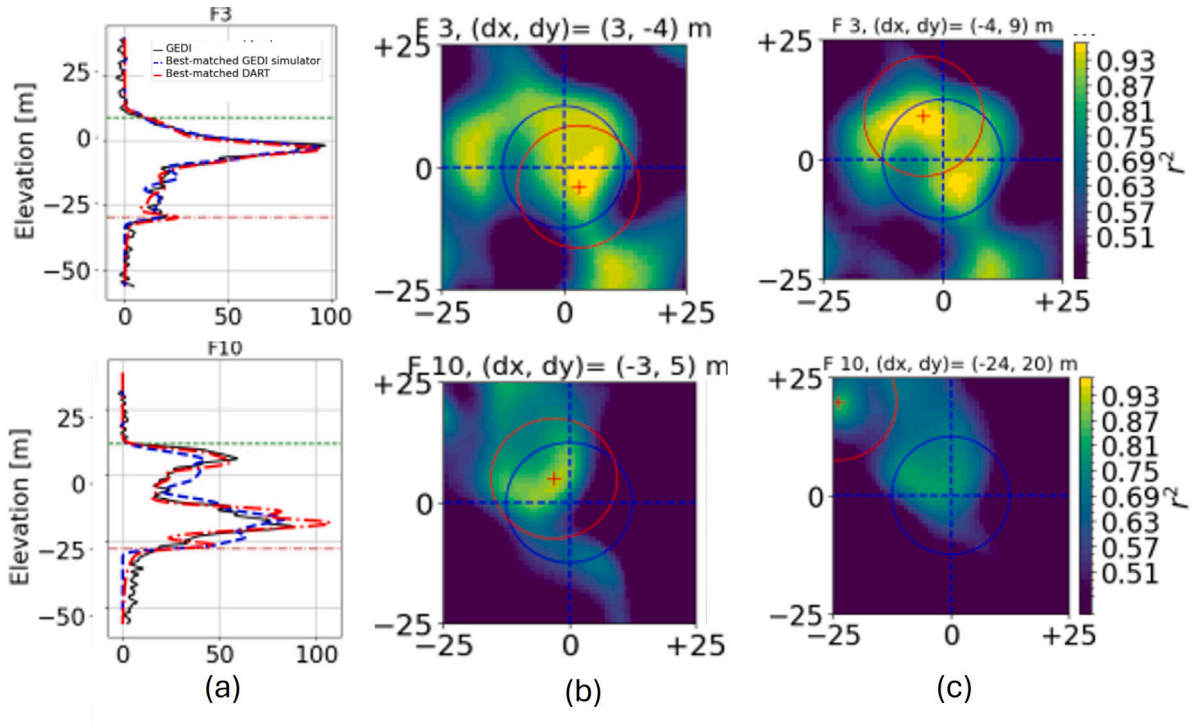

Fig. 13. Two samples (rows) of DART and GEDI Simulator results (columns a-c) for the closed canopy deciduous (SERC) site. (a) Each panel shows the observed GEDI waveform (black), the best-matched simulated waveforms from DART (red) and the GEDI Simulator (Hancock et al., 2019) (blue). (b) The corresponding correlation map for DART, (c) the corresponding correlation map for the GEDI simulator. The DART-simulated waveforms typically mimic the observed waveform more realistically, especially in cases with complex vegetation structures.

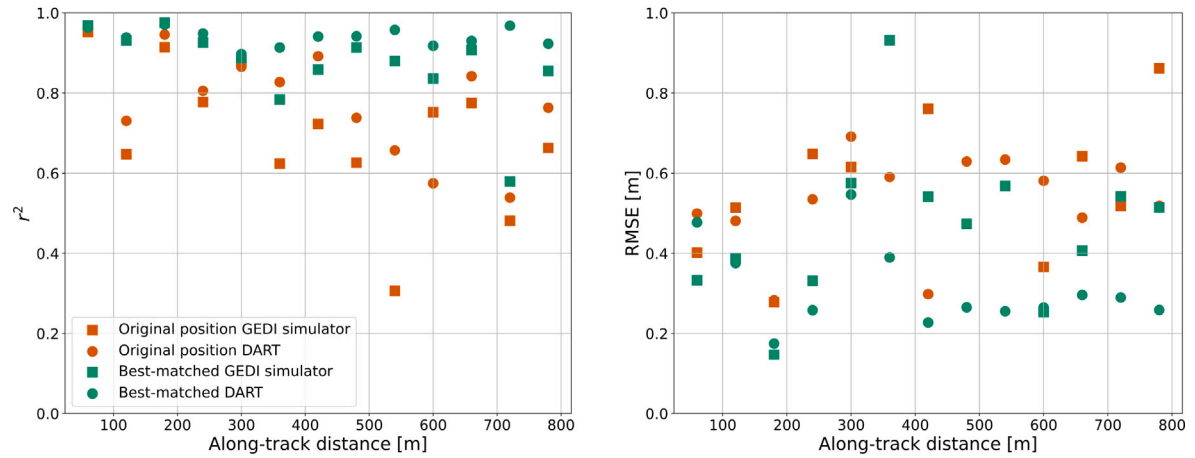

Fig. 14. Correlation coefficients and RMSE values for the observed and simulated waveforms prepared with DART and the GEDI simulator for all footprints in orbit #02273 at the closed canopy deciduous site. Note improvement in both metrics for nearly all footprints with DART best-matched waveforms.

approach is highly robust against uncertainties in canopy density estimations. While amplitude variations might theoretically be expected with changing PAD values, the normalized waveform structure, which is critical for our geolocation correction method, remains stable despite substantial variations in the assigned density values. This finding indicates that the spatial arrangement of canopy elements, rather than their precise density values, is the dominant factor influencing the characteristic shape of LiDAR waveforms within GEDI footprint. The demonstrated robustness represents a significant advantage as it eliminates the need for extremely precise PAD calibration when implementing the geolocation correction method across diverse forest ecosystems.

6.2. *Influence of canopy type on geolocation correction*

Our results underscore the significant influence of canopy type on the accuracy and reliability of GEDI geolocation evaluation and correction. In dense forests characterized by homogeneous canopies, the task of detecting and adjusting geolocation offsets for individual

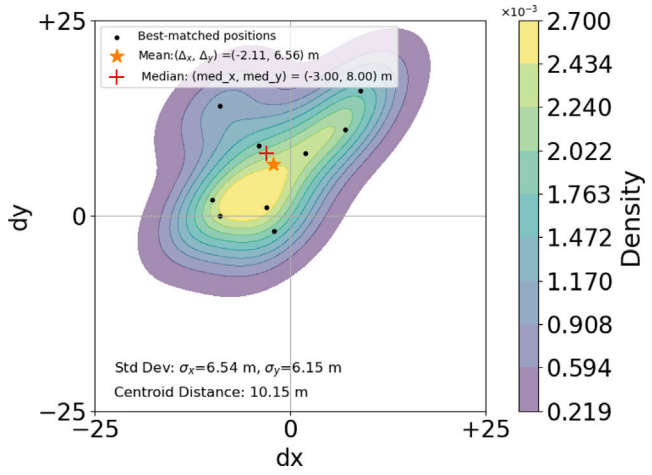

Fig. 15. Best-matched waveform positions (dx, dy) for the selected footprints at each site (black dots with annotation for corresponding footprint numbers). The orange star shows the mean offset (Δx, Δy) and the red cross shows the median offset for all footprints in the ground track. Color ramp shows point density ($pt/m2$). (For interpretation of the references to color in this figure legend, the reader is referred to the web version of this article.)

footprints proved to be particularly challenging. This difficulty stems from the similarity in the vegetation signatures across the waveforms, making it difficult to discern subtle differences in the return signal that would otherwise indicate geolocation errors. Consequently, the limited variation in canopy structure within these homogeneous environments restricts the ability to effectively differentiate and correct these offsets.

In contrast, our method demonstrated a marked improvement in heterogeneous environments, where variability in terrain and vegetation structure created more diverse waveform signatures. These differences allowed for a more precise assessment and correction of geolocation offsets, as distinct waveforms were produced for each simulation within the search space. This variability in the waveform data not only facilitated a more accurate geolocation correction, but also highlighted the importance of considering canopy structure and topographical variation when applying geolocation correction algorithms. Our approach thus offers promising potential for refining GEDI data, particularly in more complex and variable landscapes where other methods may struggle.

6.3. Influence of terrain type on geolocation correction

Geolocation accuracy is influenced by terrain characteristics, with both flat and complex topography affecting the correction process in distinct ways. In flat terrain, geolocation correction can be challenging because the waveforms from different footprints show similar ground returns. This lack of variation in the waveforms makes it difficult to effectively assess and adjust geolocation offsets, as the returned signals do not provide sufficient detail to distinguish between slight positional errors.

On the other hand, complex terrain can introduce more variation in the detected ground returns within the waveform, which can indirectly affect geolocation accuracy (Kutchartt et al., 2022). In regions with steep slopes, these variations may shift the centroid of the returned waveform, leading to systematic bias in geolocation estimates. This bias can be problematic for larger footprints where terrain variations are averaged out.

Smaller footprints, such as those in the range of 10–15 m, might help mitigate some of these issues. Smaller footprints allow for more localized analysis of the terrain, enabling more precise waveform matching and reducing the potential for terrain-induced bias geolocation corrections. This reduction in footprint size could lead to improved sensitivity to local topographic variations, enhancing the accuracy of the geolocation correction process. Therefore, a more granular approach with smaller footprints could be a key strategy for refining geolocation corrections, particularly in complex or heterogeneous landscapes.

6.4. Variability in waveform matching

Analysis across all three sites revealed notable variability in the best-matched simulated waveform positions for adjacent footprints within a single ground track. These observed offsets appear random rather than periodic, at least within the limited sample of footprints available for our study. Such randomness could be attributed to various factors, including instrument pointing errors, which we suspect contribute to the more pronounced geolocation errors observed in dense, homogeneous canopies.

Additionally, GEDI ground return data can be inaccurate, particularly in dense canopies, due to waveform attenuation and background noise. In these complex, multi-layered environments, the true ground returns are often masked, complicating accurate geolocation detection. Studies that rely solely on DSMs and ground returns may introduce biases in their assessments because these data do not account for the full range of signal interactions. In contrast, our approach leverages full-waveform data, allowing for a more comprehensive evaluation of geolocation accuracy. By accounting for vegetation returns, our method significantly improves the reliability of geolocation corrections in challenging environments, especially those with heterogeneous canopies.

6.5. Limitations and recommendations

While our study presents advances in improving geolocation accuracy at the individual footprint level, we acknowledge the limitations imposed by our relatively small sample sizes ($n < 20$) and total track lengths (<400 – 1200 m) for each site. To enhance the robustness and reliability of our geolocation corrections, we recommend expanding our study areas and considering systematic offsets across multiple GEDI beams, tracks, and orbits. This broader approach would allow for a more comprehensive understanding of the observed geolocation errors. Despite the relatively small dimensions of our simulations, there is still value in this local geolocation correction approach for more detailed analysis of GEDI and airborne LiDAR data at these sites. This local geolocation correction approach could be applied to other sites, and potentially be used to improve upon the GEDI product geolocation specification for priority science and cal/val sites. While our DART-based workflow introduces additional computational complexity, it builds upon previously validated methodologies to achieve specific research objectives. The ALS-based GEDI simulator provides a simpler, more computationally efficient alternative that is well-suited for global-scale applications. Our radiative transfer modeling approach intentionally prioritizes achieving locally accurate geolocation correction at the individual waveform level, particularly for sites where precise data fusion with other georeferenced datasets is required. This represents a fundamental trade-off between computational efficiency and precision that researchers must consider when selecting appropriate methodologies for GEDI data processing. The computational demands of our approach currently limit its applicability to targeted study sites rather than mission-scale processing, though continued advances in computing capabilities may eventually mitigate this limitation.

Future work could broaden the application of our method for larger geographic regions. Currently, there are limitations for performing large-area DART simulations due to computational and memory resources, but ongoing efforts are focused on optimizing algorithms to accommodate larger areas and more complex scene reconstructions. The new DART LiDAR mode (Yang et al., 2022) should offer improved

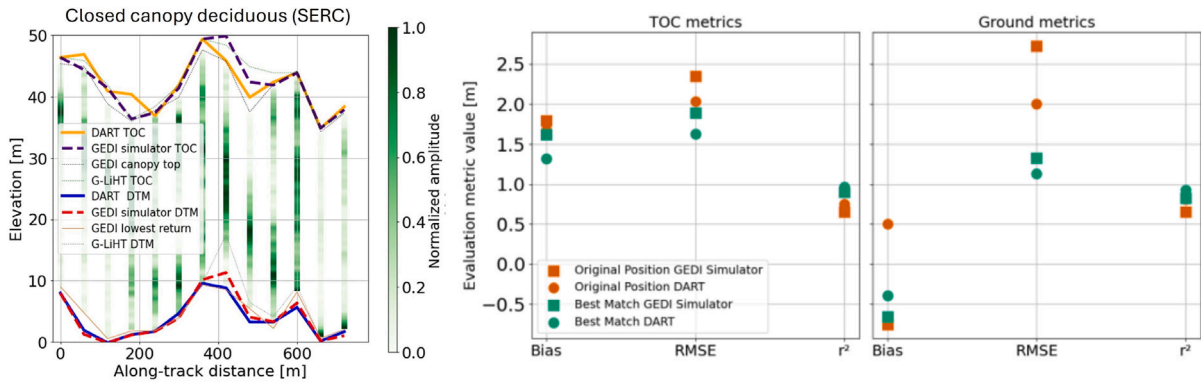

Fig. 16. GEDI Level-1B waveform density profiles and Level-2B canopy top and lowest mode (ground surface) values for the closed-canopy deciduous (SERC) site. The left panel shows the GEDI waveform profile along with different top of canopy (TOC) and digital terrain model (DTM) curves derived from G-LiHT, sampled at best-matched waveform positions from DART and the GEDI simulator. The center and right panels present metrics quantifying the differences between GEDI Level-2B values and the reference G-LiHT values, comparing original positions and best-matched waveform positions from both simulators. See Fig. 3 for G-LiHT samples at the original GEDI footprint positions.

computational efficiency. Although we accounted for seasonal consistency by selecting leaf-on ALS acquisitions, the time lag between GEDI and ALS data remains a potential limitation. Although deciduous forests in SERC exhibit minimal structural change over short time intervals, longer observational time gaps in coniferous forests could introduce uncertainties in canopy structure. Coniferous forests generally experience slow growth, reducing the likelihood of significant structural discrepancies; however, near-contemporaneous GEDI and G-LiHT acquisitions would further improve waveform simulation accuracy. Future studies could mitigate this limitation by incorporating multi-temporal ALS datasets, such as those provided for NEON sites, to track more gradual forest dynamics and refine vegetation change representation. Additionally, integrating growth models could help account for structural evolution over time and enhance the robustness of waveform simulation. Many applications require fusion of satellite laser altimetry data with other georeferenced data like point clouds from very-high-resolution satellite stereo images or airborne LiDAR to refine 3D vegetation structure estimates. Failure to address satellite altimetry geolocation errors at the individual footprint scale will negatively impact subsequent fusion efforts, potentially introducing errors in fused output products. While our current approach relies on filtering for high-quality waveforms, future work examining GEDI data in more challenging environments (e.g., extremely dense forests with significantly attenuated ground returns) might benefit from advanced signal processing techniques. The blind source separation approach described by Chang et al. (2022) offers a promising direction for separating vegetation signatures from noise in low-SNR scenarios, which could extend geolocation correction capabilities to a broader range of GEDI observations.

7. Conclusion

We developed a new method to evaluate and correct geolocation errors in full-waveform satellite laser altimetry data. Our approach used the DART model to reconstruct vegetation scenes via the PVlad model and simulate physically-realistic waveforms within a search space. Subsequently, we employed a full-waveform matching method between the simulated and observed GEDI waveforms to identify the positions of the best-matched footprint positions, offering refined geolocation accuracy.

We applied this methodology to multiple GEDI observations across different canopy types at three sites. The selection of the three study sites, representing closed canopy conifer, open canopy conifer, and closed canopy deciduous forests, enables us to constrain and evaluate the results across a range of structurally distinct forest types. This diversity ensures that the method is robust to different canopy architectures and not limited to a single forest condition. As such, the approach serves as a transferable tool that can be applied to other forested regions.

We conducted analyses at the individual GEDI footprint level and also evaluated systematic geolocation error for all footprints within each GEDI ground track. We show agreement between the best-matched simulated and observed GEDI waveforms, with $r^2 \in [0.92, 0.96]$ for the closed canopy deciduous, $r^2 \in [0.95, 0.99]$ for the closed canopy conifer, and $r^2 \in [0.93, 0.97]$ for the open canopy conifer sites. Our findings document a random distribution of GEDI geolocation errors for individual footprints at each site. We also observe systematic geolocation error of several meters for each of the GEDI tracks.

The precision of our geolocation refinement approach is influenced by various canopy and terrain characteristics at each site, including canopy type (conifer vs. deciduous), canopy roughness, 3D vertical structure, terrain roughness, and the presence of roads. We observed improved geolocation refinement accuracy for heterogeneous canopies, which generate distinct simulated waveforms for each location within the search space. In contrast, closed, dense, and homogeneous canopies presented challenges during waveform matching.

These findings highlight the ability of 3D radiative transfer models like DART to accurately simulate GEDI waveforms, with potentially improved results over empirical or semi-empirical models like the GEDI Simulator (Hancock et al., 2019). Additionally, our correlation values are derived from full-waveform matching, which entails comparing the complete waveform rather than only focusing on the ground return or specific derived metrics. Our approach leverages information from both canopy and ground signatures, which is less impacted by discrepancies in the acquisition season of the various laser altimetry datasets (i.e., leaf-off vs. leaf-on).

These advances contribute to the broader effort of spaceborne data fusion by facilitating the precise integration of vertical structure profiles from LiDAR with horizontal canopy structures and surface topography. This integration is critical for producing more accurate 3D models, particularly in heterogeneous environments where variations in canopy and terrain are pronounced.

Furthermore, our method offers potential benefits for other past, present and future laser altimeter instruments and associated data fusion efforts, including ongoing simulations to better define and understand requirements for the prioritized Surface Topography and Vegetation targeted observable (Donnellan et al., 2021) for the next NASA Decadal Survey.

CRediT authorship contribution statement

Ameni Mkaouar: Writing – original draft, Software, Methodology. **David Shean:** Writing – review & editing, Supervision, Project administration, Methodology, Conceptualization. **Tiangyang Yin:** Writing –

review & editing, Methodology. **Christopher S.R. Neigh:** Writing – review & editing, Supervision, Project administration. **Rodrigo Vieira Leite:** Software. **Paul M. Montesano:** Writing – review & editing, Supervision. **Abdelaziz Kallel:** Writing – review & editing, Methodology. **Jean-Phillipe Gastellu-Etchegorry:** Writing – review & editing.

Declaration of competing interest

The authors declare that they have no known competing financial interests or personal relationships that could have appeared to influence the work reported in this paper.

Acknowledgments

This work was supported by the NASA Decadal Survey Incubation program grant number NNH21ZDA001N-DSI. RVL was supported by an appointment to the NASA Postdoctoral Program at the Goddard Space Flight Center, administered by Oak Ridge Associated Universities under contract with NASA. Thank you for the questions and comments from the referees that helped improve the presentation and content of our study.

Appendix A. Supplementary data

Supplementary material related to this article can be found online at https://doi.org/10.1016/j.srs.2025.100248.

Data availability

The GEDI Level 1B and 2B data (Version 002) were obtained from NASA's Land Processes Distributed Active Archive Center (LP DAAC).

G-LiHT data were obtained from https://gliht.gsfc.nasa.gov/.

DART licenses are for research and teaching activities provided freely by the Paul Sabatier University (France) (www.cesbio.ups-tlse.fr/dart).

References

Béland, M., Baldocchi, D.D., 2021. Vertical structure heterogeneity in broadleaf forests: Effects on light interception and canopy photosynthesis. Agricult. Forest. Meterol. 307, 108525.

Biondi, F., 1996. Decadal-scale dynamics at the Gus Pearson natural areas: evidence for inverse asymmetric competition. Can. J. Forest Res. 26, 1397–1406. http://dx.doi.org/10.1139/x26-156.

Blair, J.B., Hofton, M.A., 1999. Modeling laser altimeter return waveforms over complex vegetation using high-resolution elevation data. Geophys. Res. Lett. 26, 2509–2512. http://dx.doi.org/10.1029/1999GL010484.

Chang, S., Deng, Y., Zhang, Y., Zhao, Q., Wang, R., Zhang, K., 2022. An advanced scheme for range ambiguity suppression of spaceborne sar based on blind source separation. IEEE Trans. Geosci. Remote Sens. 60, 1–12. http://dx.doi.org/10.1109/TGRS.2022.3184709.

Chartrand, .A.M., Howat, I.M., 2023. A comparison of contemporaneous airborne altimetry and ice-thickness measurements of antarctic ice shelves. J. Glaciol. 1–14. http://dx.doi.org/10.1017/jog.2023.49.

Chauve, A., Mallet, C., Bretar, F., Durrieu, S., Pierrot-Deseilligny, M., Puech, W., 2007. Processing full-waveform lidar data: modelling raw signals. In: ISPRS Workshop Laser Scanning and SilviLaser (LS SL). pp. 102–107.

Crockett, E.T.H., Atkins, J.W., Guo, Q., Sun, G., Potter, K.M., Ollinger, S., Silva, C.A., Tang, H., Woodall, C.W., Holgerson, J., Xiao, J., 2023. Structural and species diversity explain aboveground carbon storage in forests across the United states: Evidence from GEDI and forest inventory data. Remote Sens. Environ. 295, 113703. http://dx.doi.org/10.1016/j.rse.2023.113703.

Dennehy, C.J., Alvarez-Salazar, O.S., 2019. A survey of the spacecraft line-of-sight jitter problem. In: AAS Annual Guidance and Control Conference.

Donnellan, A., Harding, D., Lundgren, P., Wessels, K., Gardner, A., Simard, M., Parrish, C., Jones, C., Lou, Y., Stoker, J., Ranson, K., Osmanoglu, B., Lavalle, M., Luthcke, S., Saatchi, S., Treuhaft, R., 2021. Observing earth's changing surface topography and vegetation structure. https://smd-cms.nasa.gov/wp-content/uploads/2023/06/STV_Study_Report_20210622.pdf.

Dubayah, R., Armston, J., Healey, S.P., Bruening, J.M., Patterson, P.L., Kellner, J.R., Duncanson, L., Saarela, S., Ståhl, G., Yang, Z., Tang, H., Blair, J.B., Fatoyinbo, L., Goetz, S., Hancock, S., Hansen, M., Hofton, M., Hurtt, G., Luthcke, S., 2022. GEDI launches a new era of biomass inference from space. Environ. Res. Lett. 17, 095001. http://dx.doi.org/10.1088/1748-9326/ac8694.

Dubayah, R., Blair, J.B., Goetz, S., Fatoyinbo, L., Hansen, M., Healey, S., Hofton, M., Hurtt, G., Kellner, J., Luthcke, S., Armston, J., Tang, H., Duncanson, L., Hancock, S., Jantz, P., Marselis, S., Patterson, P.L., Qi, W., Silva, C., 2020a. The global ecosystem dynamics investigation: High-resolution laser ranging of the earth's forests and topography. Sci. Remote. Sens. 1, 100002. http://dx.doi.org/10.1016/j.srs.2020.100002.

Dubayah, R., Luthcke, S., Hofton, M., Blair, J., 2020b. GEDI waveform ATBD v001. http://dx.doi.org/10.5067/DOC/GEDI/GEDI_WF_ATBD.001.

Dubayah, R., Tang, H., Armston, J., Luthcke, S., Hofton, M., Blair, J., 2021. GEDI L2B canopy cover and vertical profile metrics data global footprint level v002. http://dx.doi.org/10.5067/GEDI/GEDI02_B.002.

Durrieu, S., Cherchali, S., Costeraste, J., Mondin, L., Debise, H., Chazette, P., Dauzat, J., Gastellu-Etchegorry, J.P., Baghdadi, N., Pélissier, R., 2013. Preliminary studies for a vegetation ladar/lidar space mission in france. In: 2013 IEEE International Geoscience and Remote Sensing Symposium-IGARSS. IEEE, pp. 4332–4335. http://dx.doi.org/10.1109/IGARSS.2013.6723793.

Fayad, I., Baghdadi, N., Bailly, J.S., Frappart, F., Zribi, M., 2020. Analysis of gedi elevation data accuracy for inland waterbodies altimetry. Remote. Sens. 12, 2714. http://dx.doi.org/10.3390/rs12172714.

Gastellu-Etchegorry, J.P., Demarez, V., Pinel, V., Zagolski, F., 1996. Modeling radiative transfer in heterogeneous 3-D vegetation canopies. Remote Sens. Environ. 58, 131–156. http://dx.doi.org/10.1016/0034-4257(95)00253-7.

Gastellu-Etchegorry, J.P., Lauret, N., Yin, T., Landier, L., Kallel, A., Malenovský, Z., Bitar, A.A., Aval, J., Benhmida, S., Qi, J., Medjdoub, G., Guilleux, J., Chavanon, E., Cook, B., Morton, D., Chrysoulakis, N., Mitraka, Z., 2017. DART: Recent advances in remote sensing data modeling with atmosphere, polarization, and chlorophyll fluorescence. IEEE J. Sel. Top. Appl. Earth Obs. Remote. Sens. 10, 2640–2649. http://dx.doi.org/10.1109/JSTARS.2017.2685528.

Gastellu-Etchegorry, J.P., Yin, T., Lauret, N., Grau, E., Rubio, J., Cook, B.D., Morton, D.C., Sun, G., 2016. Simulation of satellite, airborne and terrestrial lidar with DART (i): Waveform simulation with quasi-Monte Carlo ray tracing. Remote Sens. Environ. 184, 418–435. http://dx.doi.org/10.1016/j.rse.2016.07.010.

Govaerts, Y.M., Verstraete, M.M., 1998. Raytran: A monte carlo ray-tracing model to compute light scattering in three-dimensional heterogeneous media. IEEE Trans. Geosci. Remote Sens. 36, 493–505.

Hancock, S., Armston, J., Hofton, M., Sun, X., Tang, H., Duncanson, L.I., Kellner, J.R., Dubayah, R., 2019. The GEDI simulator: A large-footprint waveform lidar simulator for calibration and validation of spaceborne missions. Earth Space Sci. 6, 294–310. http://dx.doi.org/10.1029/2018EA000506.

Hmida, S.B., Kallel, A., Gastellu-Etchegorry, J.P., Roujean, J.L., 2017. Crop biophysical properties estimation based on lidar full-waveform inversion using the dart rtm. IEEE J. Sel. Top. Appl. Earth Obs. Remote. Sens. 10, 4853–4868.

Hollinger, D., Davidson, E., Fraver, S., Hughes, H., Lee, J., Richardson, A., Savage, K., Sihi, D., Teets, A., 2021. Multi-decadal carbon cycle measurements indicate resistance to external drivers of change at the howland forest ameriflux site. J. Geophys. Res.: Biogeosciences 126, e2021JG006276.

Kamoske, A.G., Dahlin, K.M., Stark, S.C., Serbin, S.P., 2019. Leaf area density from airborne LiDAR: Comparing sensors and resolutions in a temperate broadleaf forest ecosystem. Forest Ecol. Manag. 433, 364–375. http://dx.doi.org/10.1016/j.foreco.2018.11.017.

Kutchartt, E., Pedron, M., Pirotti, F., 2022. Assessment of canopy and ground height accuracy from gedi lidar over steep mountain areas. ISPRS Ann. Photogramm. Remote. Sens. Spat. Inf. Sci. V-3, 431–438. http://dx.doi.org/10.5194/isprs-annals-V-3-2022-431-2022.

Lach, S.R., Brown, S.D., Kerekes, J.P., 2006. Semi-automated dirsig scene modeling from 3d lidar and passive imaging sources. In: Laser Radar Technology and Applications XI. SPIE, pp. 161–172.

Magruder, L.A., Farrell, S.L., Neuenschwander, A., Duncanson, L., Csatho, B., Kacimi, S., Fricker, H.A., 2024. Monitoring earth's climate variables with satellite laser altimetry. Nat. Rev. Earth Environ. 1–17. http://dx.doi.org/10.1038/s43017-023-00508-8.

Magruder, L., Neuenschwander, A., Klotz, B., 2021. Digital terrain model elevation corrections using space-based imagery and icesat-2 laser altimetry. Remote Sens. Environ. 264, 112621. http://dx.doi.org/10.1016/j.rse.2021.112621.

Menounos, B., Gardner, A., Forentine, C., Fountain, A., 2023. Brief communication: Recent estimates of glacier mass loss for western north america from laser altimetry. EGUsphere 2023, 1–10. http://dx.doi.org/10.5194/tc-18-889-2024.

Musthafa, M., Singh, G., Kumar, P., 2023. Comparison of forest stand height interpolation of gedi and icesat-2 lidar measurements over tropical and sub-tropical forests in india. Environ. Monit. Assess. 195, 71. http://dx.doi.org/10.1007/s10661-022-10657-w.

Ni-Meister, W., Jupp, D.L., Dubayah, R., 2001. Modeling lidar waveforms in heterogeneous and discrete canopies. IEEE Trans. Geosci. Remote Sens. 39, 1943–1958. http://dx.doi.org/10.1109/36.951085.

Ni-Meister, W., Yang, W., Kiang, N.Y., 2010. A clumped-foliage canopy radiative transfer model for a global dynamic terrestrial ecosystem model. i: Theory. Agricult. Forest. Meterol. 150, 881–894.

Qin, H., Wang, C., Xi, X., Tian, J., Zhou, G., 2017. Simulating the effects of the airborne lidar scanning angle, flying altitude, and pulse density for forest foliage profile retrieval. Appl. Sci. 7, 712. http://dx.doi.org/10.3390/app7070712.

Regaieg, O., Yin, T., Malenovský, Z., Cook, B.D., Morton, D.C., Gastellu-Etchegorry, J.P., 2021. Assessing impacts of canopy 3D structure on chlorophyll fluorescence radiance and radiative budget of deciduous forest stands using DART. Remote Sens. Environ. 265, 112673. http://dx.doi.org/10.1016/j.rse.2021.112673.

Roy, D.P., Kashongwe, H.B., Armston, J., 2021. The impact of geolocation uncertainty on GEDI tropical forest canopy height estimation and change monitoring. Sci. Remote. Sens. 4, 100024. http://dx.doi.org/10.1016/j.srs.2021.100024.

Schleich, A., Durrieu, S., Soma, M., Vega, C., 2023. Improving GEDI footprint geolocation using a high-resolution digital elevation model. IEEE J. Sel. Top. Appl. Earth Obs. Remote. Sens. 16, 7718–7732. http://dx.doi.org/10.1109/JSTARS.2023.3298991, conference Name: IEEE Journal of Selected Topics in Applied Earth Observations and Remote Sensing.

Schneider, F.D., Ferraz, A., Hancock, S., Duncanson, L.I., Dubayah, R.O., Pavlick, R.P., Schimel, D.S., 2020. Towards mapping the diversity of canopy structure from space with GEDI. Environ. Res. Lett. 15, 115006. http://dx.doi.org/10.1088/1748-9326/ab9e99.

Shean, D., Bhushan, S., Smith, B., Besso, H., Sutterley, T., Swinski, J.P., Henderson, S., Neumann, T., Williams, J., 2021. Evaluating and improving seasonal snow depth retrievals with satellite laser altimetry. In: AGU Fall Meeting Abstracts. pp. C33B–04.

Sihi, D., Davidson, E.A., Chen, M., Savage, K.E., Richardson, A.D., Keenan, T.F., Hollinger, D.Y., 2018. Merging a mechanistic enzymatic model of soil heterotrophic respiration into an ecosystem model in two ameriflux sites of northeastern usa. Agricult. Forest. Meterol. 252, 155–166. http://dx.doi.org/10.1016/j.agrformet.2018.01.026.

Sun, M., Cui, L., Park, J., García, M., Zhou, Y., Silva, C.A., He, L., Zhang, H., Zhao, K., 2022. Evaluation of nasa's GEDI lidar observations for estimating biomass in temperate and tropical forests. Forests 13, 1686. http://dx.doi.org/10.3390/f13101686.

Tang, H., Stoker, J., Luthcke, S., Armston, J., Lee, K., Blair, B., Hofton, M., 2023. Evaluating and mitigating the impact of systematic geolocation error on canopy height measurement performance of GEDI. Remote Sens. Environ. 291, 113571. http://dx.doi.org/10.1016/j.rse.2023.113571.

Wang, C., Yang, X., Xi, X., Zhang, H., Chen, S., Peng, S., Zhu, X., 2020. Evaluation of footprint horizontal geolocation accuracy of spaceborne full-waveform lidar based on digital surface model. IEEE J. Sel. Top. Appl. Earth Obs. Remote. Sens. 13, 2135–2144. http://dx.doi.org/10.1109/JSTARS.2020.2992094.

Wei, S., Yin, T., Dissegna, M.A., Whittle, A.J., Ow, G.L.F., Yusof, M.L.M., Lauret, N., Gastellu-Etchegorry, J.P., 2020. An assessment study of three indirect methods for estimating leaf area density and leaf area index of individual trees. Agricult. Forest. Meterol. 292, 108101. http://dx.doi.org/10.1016/j.agrformet.2020.108101.

Widlowski, J.L., Mio, C., Disney, M., Adams, J., Andredakis, I., Atzberger, C., Brennan, J., Busetto, L., Chelle, M., Ceccherini, G., et al., 2015. The fourth phase of the radiative transfer model intercomparison (rami) exercise: Actual canopy scenarios and conformity testing. Remote Sens. Environ. 169, 418–437. http://dx.doi.org/10.1016/j.rse.2015.08.016.

Xu, Y., Ding, S., Chen, P., Tang, H., Ren, H., Huang, H., 2023a. Horizontal geolocation error evaluation and correction on full-waveform LiDAR footprints via waveform matching. Remote. Sens. 15, 776. http://dx.doi.org/10.3390/rs15030776.

Xu, Y., Ding, S., Chen, P., Tang, H., Ren, H., Huang, H., 2023b. Horizontal geolocation error evaluation and correction on full-waveform lidar footprints via waveform matching. Remote. Sens. 15, 776.

Yang, X., Wang, Y., Yin, T., Wang, C., Lauret, N., Regaieg, O., Xi, X., Gastellu-Etchegorry, J.P., 2022. Comprehensive LiDAR simulation with efficient physically-based DART-lux model (i): Theory novelty, and consistency validation. Remote Sens. Environ. 272, 112952. http://dx.doi.org/10.1016/j.rse.2022.112952.

Yin, T., Cook, B.D., Morton, D.C., 2022. Three-dimensional estimation of deciduous forest canopy structure and leaf area using multi-directional, leaf-on and leaf-off airborne lidar data. Agricult. Forest. Meterol. 314, 108781. http://dx.doi.org/10.1016/j.agrformet.2021.108781.

Yin, T., Lauret, N., Gastellu-Etchegorry, J.P., 2016. Simulation of satellite, airborne and terrestrial LiDAR with DART (II): ALS and TLS multi-pulse acquisitions, photon counting, and solar noise. Remote Sens. Environ. 184, 454–468. http://dx.doi.org/10.1016/j.rse.2016.07.009.

Yin, T., Montesano, P.M., Cook, B.D., Chavanon, E., Neigh, C.S., Shean, D., Peng, D., Lauret, N., Mkaouar, A., Morton, D.C., et al., 2023. Modeling forest canopy surface retrievals using very high-resolution spaceborne stereogrammetry:(i) methods and comparisons with actual data. Remote Sens. Environ. 298, 113825.

Zhang, Z., Bo, Y., Jin, S., Chen, G., Dong, Z., 2023. Dynamic water level changes in qinghai lake from integrating refined icesat-2 and gedi altimetry data (2018–2021). J. Hydrol. 617, 129007. http://dx.doi.org/10.1016/j.jhydrol.2022.129007.